Drivers of spatio-temporal variability of carbon dioxide and energy fluxes in a Mediterranean savanna ecosystem

Tarek S. El-Madany[a,*], Markus Reichstein[a], Oscar Perez-Priego[a], Arnaud Carrara[b], Gerardo Moreno[c], M. Pilar Martín[d], Javier Pacheco-Labrador[a,d], Georg Wohlfahrt[e], Hector Nieto[f], Ulrich Weber[a], Olaf Kolle[a], Yun-Peng Luo[a], Nuno Carvalhais[a,g], Mirco Migliavacca[a]

[a] Max Planck Institute for Biogeochemistry Department Biogeochemical Integration, Germany
[b] Centro de Estudios Ambientales del Mediterráneo (CEAM), Valencia, Spain
[c] Forest Research Group – INDEHESA University of Extremadura, Plasencia, Spain
[d] Environmental Remote Sensing and Spectroscopy (SpecLab), Spanish National Research Council, Madrid, Spain
[e] University of Innsbruck – Institute of Ecology, Austria
[f] Efficient Use of Water Program, IRTA – Research & Technology Food & Agriculture, Fruitcentre, Parc Cientific i Tecnològic Agroalimentari (PCiTAL), Lleida, 25003, Spain
[g] CENSE, Departamento de Ciências e Engenharia do Ambiente, Faculdade de Ciências e Tecnologia, Universidade NOVA de Lisboa, Caparica, 2829-516, Portugal

ARTICLE INFO

ABSTRACT

To understand what is driving spatial flux variability within a savanna type ecosystem in central Spain, data of three co-located eddy covariance (EC) towers in combination with hyperspectral airborne measurements and footprint analysis were used. The three EC systems show consistent, and unbiased mass and energy fluxes. Nevertheless, instantaneous between-tower flux differences i.e. paired half hourly fluxes, showed large variability. A period of 13 days around an airborne hyperspectral campaign was analyzed and proved that between-tower differences can be associated to biophysical properties of the sampled footprint areas. At high photosynthetically active radiation (PAR) net ecosystem exchange (NEE) was mainly controlled by chlorophyll content of the vegetation (estimated through MERIS Terrestrial Chlorophyll Index (MTCI)), while sensible heat flux (H) was driven by surface temperature. The spatial variability of biophysical properties translates into flux variability depending on the location and size of footprints. For H, negative correlations were found with surface temperature for between-tower differences, and for individual towers in time, meaning that higher H was observed at lower surface temperatures. High aerodynamic conductance of tree canopies reduces the canopy surface temperature and the excess energy is relieved as H. Therefore, higher tree canopy fractions yielded to lower surface temperatures and at the same time to higher H. For NEE, flux differences between towers were correlated to differences in MTCI of the respective footprints, showing that higher chlorophyll content of the vegetation translates into more photosynthetic CO_2 uptake, which controls NEE variability. Between-tower differences of latent heat fluxes (LE) showed no consistent correlation to any vegetation index (VI), or structural parameter e.g. tree-grass-fraction. This missing correlation is most likely caused by the large contribution of soil evaporation to ecosystem LE, which is not captured by any of the biophysical and structural properties.

To analyze if spatial heterogeneity influences the uncertainty of measured fluxes three different measures of uncertainty were compared: the standard deviation of the marginal distribution sampling (MDS), the two-tower-approach (TTA), and the variance of the covariance (RE). All three uncertainty estimates had similar means and distributions at the individual towers while the methods were significantly different to each other. The uncertainty estimates increased from RE over TTA to MDS, indicating that different components like space, time, meteorology, and phenology are factors, which affect the uncertainty estimates. Differences between uncertainty estimates from the RE and TTA indicate that spatial heterogeneity contributes significantly to the ecosystem-flux uncertainty.

* Corresponding author at: Biosphere-Atmosphere Interactions and Experimentation Group, Biogeochemical Integration Department, Max Planck Institute for Biogeochemistry, Hans-Knöll-Str. 10, 07745, Jena, Germany.
E-mail address: telmad@bgc-jena.mpg.de (T.S. El-Madany).

1. Introduction

Savanna type ecosystems play an important role in global carbon stocks and their productivity (Ahlstrom et al., 2015; Grace et al., 2006), they are highly variable in seasonal carbon and water vapor fluxes (Eamus et al., 2013; Paço et al., 2009; Tagesson et al., 2015; Unger et al., 2012) and inter-annual (Chen et al., 2016; Costa-e-Silva et al., 2015; Dubbert et al., 2014; Ma et al., 2007; Nagler et al., 2007; Pereira et al., 2007) time scales. Savannas are complex ecosystems which consist of scattered trees and a coexisting continuous grass layer/understory (Scholes and Archer, 1997). The relative contribution of trees and the understory to overall ecosystem fluxes experience strong seasonal variations, and can vary substantially depending on the savanna type and its characteristics (e.g. Dubbert et al., 2014; Moore et al., 2016; Otieno et al., 2015; Paço et al., 2009). Within a savanna ecosystem, the spatial distribution of trees and the composition of the understory can result in spatial heterogeneity of biophysical properties and ultimately fluxes. To determine spatial flux heterogeneity on the ecosystem scale, flux footprint models offer a great possibility as they allow relating flux measurements and therefore flux variability, to surface properties. When detailed spatial information on surface characteristics are available for the footprint area, they can be utilized to explain spatial flux variability. Due to the intrinsic uncertainties associated with the eddy covariance (EC) technique, the observed variability in flux measurements is not entirely related to spatial heterogeneity. Rannik et al. (2016) reviewed different flux error estimates for EC measurements and compared their values for different ecosystems. They suggested to use the method proposed by Finkelstein and Sims (2001) or Wienhold et al. (1995) to estimate the random uncertainty of turbulent flux measurements. Both methods can be used to associate uncertainties to each individual flux averaging period. These uncertainty estimates account for the properties of the measured time series (vertical wind speed and scalar of interest), but do not integrate information about the observed variability in flux measurements observed under similar meteorological conditions and phenological stages. Two widely used methods to quantify this uncertainty are the standard deviation of the marginal distribution sampling (MDS; Reichstein et al., 2005) and the two-tower-approach (TTA; Hollinger and Richardson, 2005; Kessomkiat et al., 2013). The MDS is based on the assumption that, for a short time window and under the same meteorological conditions, fluxes should be similar. The TTA uses two co-located towers (i.e. a few hundred meters apart), which are sampling independent areas of the same homogeneous ecosystem and compares the differences of the simultaneous flux measurements. For the TTA differences in meteorological conditions are (nearly) completely eliminated and differences in phenological stage and biophysical properties should be minimized. Nevertheless, biophysical properties within the footprint area (Schmid, 2002) can change spatially and, therefore, influence flux measurements and increase the uncertainty estimate. High spatial resolution remote/proximal sensing provides means to better characterize and quantify spatial heterogeneity. For example, Balzarolo et al. (2015) and Perez-Priego et al. (2015) showed for grasslands, that variability in measured CO_2-fluxes can be related to changes in vegetation indices (VIs), which were derived from hyperspectral measurements. The best agreement was found between CO_2-fluxes and VIs associated to chlorophyll and water-content of the canopy, as well as sun-induced chlorophyll fluorescence. For savanna type ecosystems, where a multispecies herbaceous layer (annual grasses, forbs, and legumes) coexists with sparsely distributed trees, spatial heterogeneity of e.g. chlorophyll content of the vegetation and leaf area index (LAI) introduce a new dimension to account for. Variations of biophysical properties can occur at the herbaceous- and tree layer, or as a consequence of changes in the tree density and canopy fraction within the footprint area. From this point of view, it is not clear how representative flux measurements can be in such a complex ecosystem to represent ecosystem scale fluxes correctly. To be precise, this is not a special problem of savanna type ecosystems but to all EC-sites presenting significant variability in biophysical properties at EC footprint scale.

This work focuses on the analysis of data collected with three co-located EC flux towers within the framework of a fertilization experiment (Migliavacca et al., 2017). Here, only the data acquired before the fertilization are analyzed. The main objective is to evaluate the causes of differences between the simultaneous, half hourly flux measurements collected by the three co-located EC towers and to identify the main factors, (especially random errors vs. variability in biophysical surface properties), controlling the variability of measured carbon-, water-, and energy fluxes. For this purpose we (i) conduct a thorough uncertainty analysis including three different methods and (ii) make use of a combination of EC measurements, high resolution airborne hyperspectral information, and footprint analysis to identify spatial heterogeneity of mass and energy fluxes, and to correlate spatial flux differences with VIs derived from hyperspectral data and surface properties.

## 2. Methods

2.1. Site description

The study was carried out in the Majadas de Tietar site (Casals et al., 2009) located in western Spain (39°56′25″N 5°46′29″W). The ecosystem is a typical "Iberic Dehesa", with an herbaceous stratum of native pasture and a tree layer of scattered oak trees, with 98% of the trees being *Quercus ilex*. The tree density is about 20–25 trees ha^{-1} with a mean DBH of 46 cm and a canopy height of about 8 m. The canopy fraction of the trees is about 20%. The herbaceous layer consists mostly of various annual native species such as *Vulpia bromoides* (L.), *Vulpia geniculate* (L.), *Trifolium subterraneum* (L.), *Ornithopus compressus* (L.) with often more than 20 species within 4 m^2. The fractional cover of the three main functional plant forms within the pasture (grasses, forbs, and legumes), varies spatially but also seasonally according to their phenological status (Perez-Priego et al., 2015). The LAI of the trees is around 0.35 m^2 m^{-2} (1.5–2.0 m^{2}m^{-2} on a tree basis) while the spring peak green LAI of the herbaceous layer ranges between 0.5–2.5 m^{2}m^{-2} due to spatial heterogeneity (Migliavacca et al., 2017).

For clarity, we emphasize that the analyzed ecosystem is very heterogeneous on spatial scales of centimeters to few tens of meters with large variability in plant species and their distribution within the herbaceous layer. Trees on average are equally distributed within the ecosystem with locally more clustered and open areas. On scales of few hundreds of meters the ecosystem becomes homogeneous. This scale, at which the ecosystem is becoming homogeneous corresponds to the size of daytime flux footprints which are the basis for the analysis of this study.

The savanna is managed and used for continuous grazing of livestock with a low density of 0.3 cows ha^{-1} which is similar at all the sites. During the driest summer months (July–September) the cattle is usually moved to nearby mountain grasslands.

Mean annual temperature is 16.7 °C and annual precipitation is ca. 650 mm with large inter-annual variability. The prevailing wind directions are West-Southwest and East-Northeast (Fig. 1).

Three EC towers were operated simultaneously at the site to monitor ecosystem fluxes. The Control-Tower (CT) is the long-term eddy covariance FLUXNET site Majadas de Tietar (ES-LMa in FLUXNET, since 2003), while the other two towers (Nitrogen added Tower (NT), ES-LM1 in FLUXNET; and Nitrogen and Phosphorous added Tower (NPT), ES-LM2 in FLUXNET) were set up in March 2014 at a distance of 450 and 630 m from the CT in northwestern and southern direction, respectively (Fig. 1). The locations have been selected such that the footprints do not overlap under most frequent meteorological conditions, and that the tree cover and management around the towers are similar.
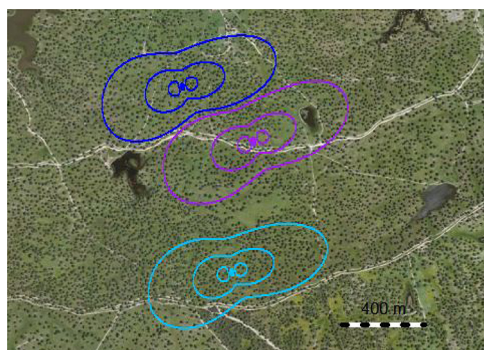
Fig. 1. 20%, 60%, and 80% iso-lines of the footprint climatology for three ecosystem towers for the period of March 2014 till January 2017. Control tower (CT) in purple, Nitrogen added tower (NT) in blue, and the nitrogen and phosphorous added tower (NPT) in light blue. Footprint climatology was calculated according to Kljun et al. (2015). (For interpretation of the references to colour in this figure legend, the reader is referred to the web version of this article).

Table 1

Vegetation indices (Normalized Difference Vegetation Index (NDVI), Enhanced Vegetation Index (EVI), Photochemical Reflectance Index (PRI), MERIS Terrestrial Chlorophyll Index (MTCI)) and their formulation. ρ are the hemispherical-directional reflectance factors for specific wavelengths, the numbers denoting the wavelengths in nm.

VI	Equation	Reference
NDVI	$NDVI = \frac{\rho_{800} - \rho_{670}}{\rho_{800} + \rho_{670}}$	Rouse et al. (1974)
EVI$_{MODIS}$	$EVI_{MODIS} = \frac{\rho_{800} - \rho_{670}}{(\rho_{800} + 6 \cdot \rho_{670} - 7.5 \cdot \rho_{469} + 1)}$	Huete et al. (2002)
PRI	$PRI = \frac{\rho_{531} - \rho_{570}}{\rho_{531} + \rho_{570}}$	Gamon et al. (1992)
MTCI	$MTCI = \frac{\rho_{753.75} - \rho_{708.5}}{\rho_{708.5} + \rho_{681.25}}$	Dash and Curran (2004)

2.2. Instrumentation and flux calculation

The EC systems were identical at each tower and consisted of a three-dimensional sonic anemometer (R3-50, Gill LTD UK) and an infrared gas analyzer to measure dry mixing ratios of CO_2 and H_2O (LI-7200, Licor Bioscience, Lincoln, USA). The measurement height was 15 m and 15.5 m above ground at NT / NPT and CT, respectively, which corresponds roughly to 7 m above the mean tree canopy height. Shortwave incoming radiation (Rg) was measured with a net radiometer (CNR4, Kipp and Zonen, Delft, Netherlands) roughly at 15 m. Temperature (Tair) and relative humidity (rH) were measured with a combined Pt-100 temperature and capacitive humidity sensor (CPK1-5, MELA Sensortechnik, Germany) at 15 m. Soil moisture (SWC) was measured at 0.1 and 0.3 m below ground (ML2x, Delat-T Devices Ltd, Cambridge, UK). Vertical CO_2 and H_2O concentration-profiles were measured at seven levels between the surface and the measurement height (0.1, 0.5, 1.0, 2.0, 5.0, 9.0, and 15 m above ground with a LI-840, Licor Bioscience, Lincoln, USA). Vertical profiles of CO_2 were measured at the NT and NPT, but not at CT. The storage term at the CT was estimated as the mean of the other two towers as the differences between profiles were negligible.

All EC raw data were collected at 20 Hz with the software EddyMeas (Kolle and Rebmann, 2009). This includes the three dimensional wind velocities (u,v,w in m s^{-1}), sonic temperature (Tson in K), and dry mixing ratios of CO_2 (μmol mol^{-1}) and H_2O (mmol mol^{-1}). Tson was internally corrected for cross wind sensitivity by the sonic anemometer. Raw data were processed with EddyPro version 5.2.0 (Fratini and Mauder, 2014). Where all raw data were despiked according to Vickers and Mahrt (1997) with linear interpolation for the detected spikes, the arithmetic mean was removed from time series, CO_2 time lags were determined by covariance maximization in predefined windows, and for water vapor the same procedure was done as a function of relative humidity. Spectral corrections included the analytical correction for high-pass and low-pass filtering effects (Moncrieff et al. (2004) and Moncrieff et al. (1997)). For the two main wind directions (East-

Table 2

Absolute values of the 25th, 50th, and 75th percentile of the normalized range of surface properties (Normalized Difference Vegetation Index (NDVI), Enhanced Vegetation Index (EVI), Photochemical Reflectance Index (PRI), MERIS Terrestrial Chlorophyll Index (MTCI), Tree-Grass-Ratio (TGR), surface temperature (T$_{sur}$)) and net ecosystem exchange (NEE) shown in Fig. 6. Values correspond to the period between April 6th – April 18th 2014. Median values are in bold for better orientation.

Variable / Tower	Percentile	CT	NT	NPT
NDVI	25	0.63	0.65	0.65
	50	**0.66**	**0.67**	**0.68**
	75	0.67	0.68	0.69
EVI	25	0.33	0.35	0.33
	50	**0.34**	**0.36**	**0.35**
	75	0.35	0.37	0.36
PRI	25	-0.0759	-0.0758	-0.0772
	50	**-0.0755**	**-0.0747**	**-0.0767**
	75	-0.0752	-0.0736	-0.0763
MTCI	25	1.67	1.78	1.76
	50	**1.72**	**1.81**	**1.81**
	75	1.80	1.83	1.84
TGR	25	0.17	0.19	0.27
	50	**0.20**	**0.21**	**0.30**
	75	0.22	0.28	0.31
T$_{sur}$	25	27.9	28.6	28.0
	50	**28.2**	**29.0**	**28.1**
	75	28.5	29.2	28.4
NEE	25	-10.2	-10.1	-10.4
	50	**-8.4**	**-8.8**	**-9.2**
	75	-6.5	-5.9	-7.4
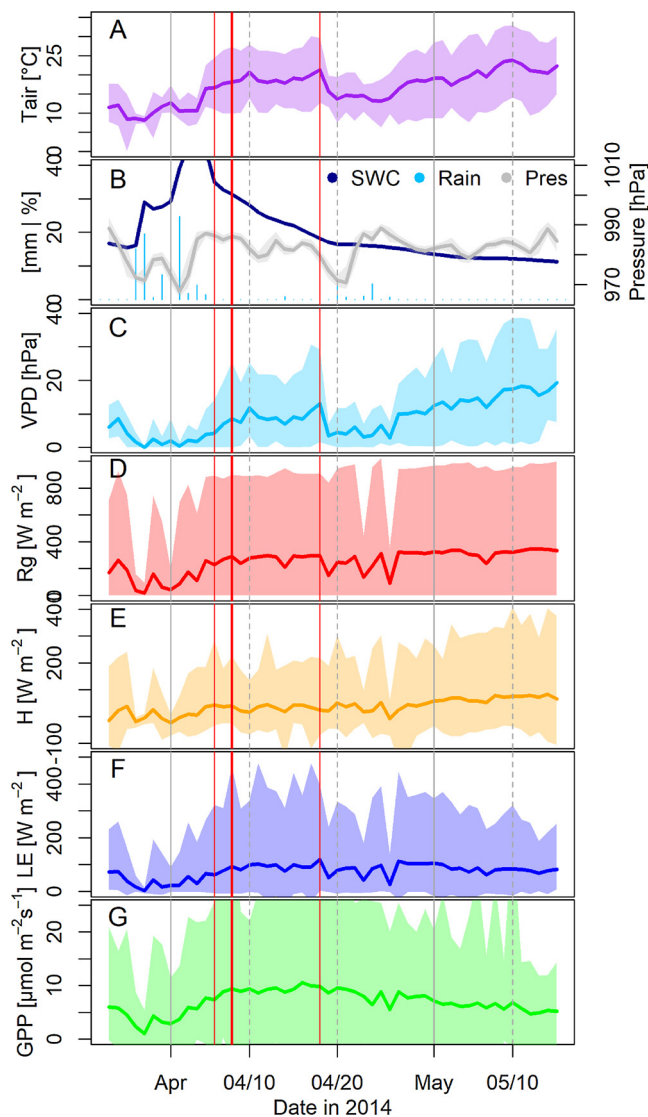
Fig. 2. Time-series of mean daily air temperature (°C) at 2 m above ground (A), volumetric soil water content (%) in 10 cm depth as well as daily sums of precipitation (mm) (B), vapor pressure deficit (VPD; hPa) calculated from temperature and relative humidity at 2 m above ground level (C), global radiation (Rg; W m^{-2}) (D), sensible heat flux (H; W m^{-2}) (E), latent heat flux (LE; W m^{-2}) (F), and gross primary productivity (GPP; μmol m^{-2} s^{-1}) (G) as measured at the nitrogen added tower. Solid lines are daily averages and shaded areas the respective minimum and maximum values calculated for each day. The thin vertical red lines mark the period around the flight (April 6th – April 18th) which was used for additional analysis; the bold red line indicates the flight day (April 8th). Grey solid lines indicate the first of each month and grey dashed lines are the 10th and 20th of each month, respectively. (For interpretation of the references to colour in this figure legend, the reader is referred to the web version of this article).

Northeast and West-Southwest) the planar fit method (Wilczak et al., 2001) was used for coordinate rotation while double rotation was applied for the other wind directions. Quality check of the calculated fluxes was done according to the 0-1-2 system (Mauder and Foken, 2011; Rebmann et al., 2005) and Vickers and Mahrt (1997). The storage flux was then computed according to Aubinet et al. (2001). For each 10 min record, a spline was fitted to the vertical profile and integrated over the temporal change to derive the storage flux between the measurement height and the surface. The mean of the three 10 min storage fluxes was used as the half hourly storage flux. The storage flux was added to the CO_2 flux to compute the net ecosystem exchange (NEE),

then, the u*-threshold (0.13 m^{-1}) was estimated (Papale et al., 2006). Bad quality data were gap-filled with MDS (Reichstein et al., 2005), and subsequently NEE was partitioned into gross primary production (GPP) and ecosystem respiration (Reco) according to the night-time partitioning method as implemented in the REddyProc 0.7-1 R package (Wutzler et al., 2018). Flux uncertainties were estimated according to three different methods. (i) The variance of the co-variance according to Finkelstein and Sims (2001), where in the original paper the term is defined to as the 'random sampling error', and hereafter referred as 'RE'. (ii) The flux uncertainty as calculated from the standard deviation of the marginal distribution sampling (MDS) of the gap-filling procedure (Reichstein et al., 2005). Finally, (iii) the two tower approach (TTA) according to Hollinger and Richardson (2005). The 'RE' is calculated for each half hourly period based on the raw time series of the vertical wind speed and the scalar of interest. The uncertainty estimate of the TTA was modified as compared to the original paper in the following way: (i) flux differences were calculated for each paired observation of flux measurements at the two towers of interest. (ii) The resulting flux differences were then included in the MDS algorithm to calculate the standard deviation of the flux differences for bins of similar meteorological conditions within a +/- seven-day window. The same bin width were used for the TTA and MDS as described in Reichstein et al. (2005) (Tair = 2.5 K, VPD = 5 hPa, Rg = 50 Wm^{-2}). Estimated uncertainties were available for each half hourly flux value. Uncertainties were used for further analysis if 10 or more values fell into a certain meteorological bin.

There are differences in the information content embedded in each of the methods used to estimate flux uncertainties:

(i) the RE method is only based on half hourly turbulent time series (e.g. vertical wind speed and CO_2) and their auto- and cross-correlation, hence containing no, or only very limited information about spatial, temporal, or meteorological variability;

(ii) the uncertainty from the TTA includes the variability coming from different instruments, which should be negligible, but is mostly dominated by the differences in the spatial variability emerging from the footprints of the two towers (given that flux differences are calculated for the same moment in time under the same meteorological conditions); and

(iii) the MDS uncertainties include information on spatial variability (given changes in the footprints between half hours), on temporal variability (given the +/− 7 days sampling window around an observation), and to a certain degree also variability in meteorological conditions (which should be relatively small given the narrow bin widths).

2.3. Airborne hyperspectral imagery

Vegetation indices and land cover classifications have been retrieved from airborne hyperspectral measurements acquired from a Compact Airborne Spectral Imager (CASI-1500i; Itres Research Ltd., Canada) over the study site on April 8th 2014 starting at 11:15 UTC. The different overpasses were used to generate a mosaic covering the study area with 1.25 m pixel size after image resampling (0.90 m across track and 1.66 along track original pixel size at nadir) using the software Geocor (Itres Research Ltd., Canada); resampling was based on the smallest off-nadir look angle and no further corrections or interpolations were applied. Spectral information was recorded on 144 bands between 380 and 1050 nm wavelengths from which spectral VIs were calculated (Table 1). Original spectral bands and derived VIs were combined to classify imagery using a supervised method based on the Mahalanobis distance (Richards, 2013). Classification and VI calculations were carried out in ENVI 5.1 and IDL 8.3.0 (Harris Geospatial Solutions, Boulder, CO, USA). Each pixel was classified as sunlit grass, shaded grass, tree canopy, bare soil, or water surface. The tree-grass ratio (TGR) was calculated as the ratio of tree canopy pixels over sunlit
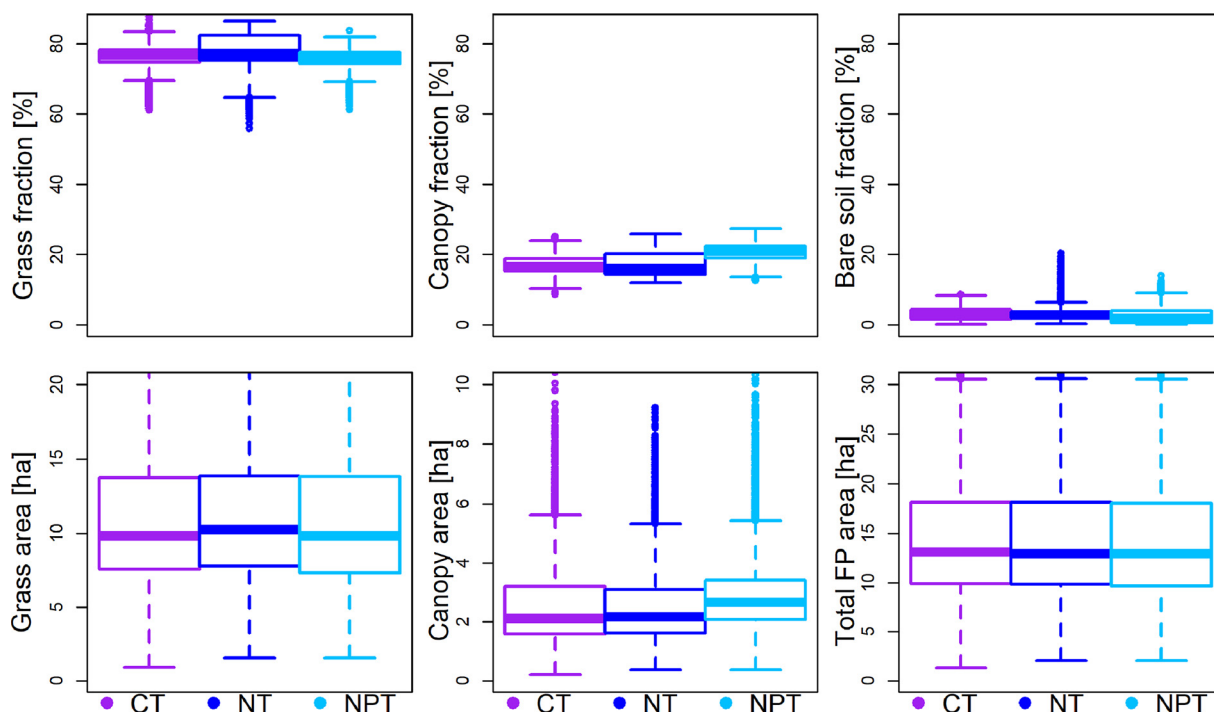
Fig. 3. Boxplots of footprint (FP) characteristics for the individual towers for the year 2014; Day- and nighttime data with u* > u*-threshold (0.13 m s^{-1}). Grass, tree, and bare soil areas were calculated by intersecting the footprints with the classification map derived from hyperspectral flight.
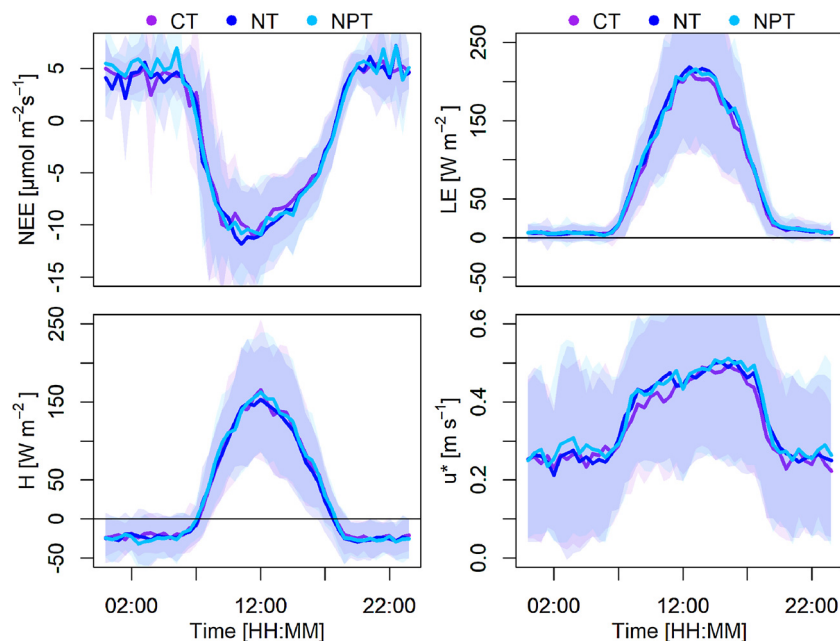

Fig. 4. Mean diurnal courses of NEE, LE, H, and u*. Solid line is mean diurnal course and shaded area is the respective standard deviation for growing period between March 25th and May 15th 2014.

and shaded grass pixels (Table 2).

Surface temperature (Tsur) was obtained from multispectral thermal infrared imagery with an Airborne Hyperspectral Scanner (AHS) using a temperature and emissivity separation algorithm (Gillespie et al., 1998; Sobrino et al., 2006). Both AHS and CASI sensors were flown simultaneously onboard the C-212-200 RS aircraft operated by the Spanish Institute for Aerospace Technology (INTA). The spatial resolution of the AHS images was ~ 4.5 m, so in order to obtain surface temperatures at a similar resolution as the hyperspectral CASI data, a Data Mining Sharpening algorithm (Gao et al., 2012) was applied by

fusing the lower resolution AHS surface temperature with the higher resolution CASI hyperspectral optical data to produce sharpened 1.5 m resolution surface temperature maps.

2.4. Footprint analysis

2.4.1. Footprint modelling

To relate measured fluxes with surface properties (i.e. land cover classification-, surface temperature- and VI-maps) two-dimensional flux footprints were calculated for each half hour using the footprint model
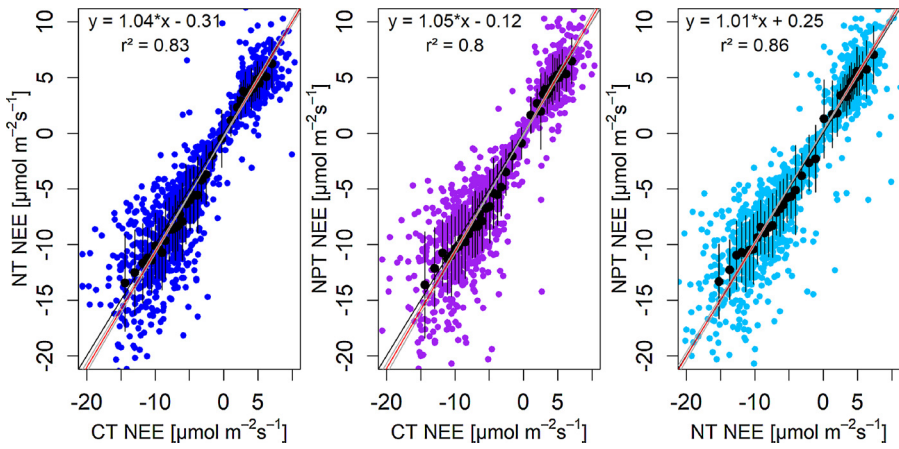
Fig. 5. Correlations of half hourly NEE [μmol m^{-2} s^{-1}] between towers for spring 2014 (March 25th and May 15th 2014). Black line is 1:1-line, red line is linear fit according to the major axis regression with the respective formula and r^2 values in the upper left corner. The grey lines represent the 2.5 and 97.5% confidence intervals of the linear fit. The full black circles and vertical lines indicate the mean and standard deviation of the y-values for each 2.5th percentile of the respective x-values. (For interpretation of the references to colour in this figure legend, the reader is referred to the web version of this article).
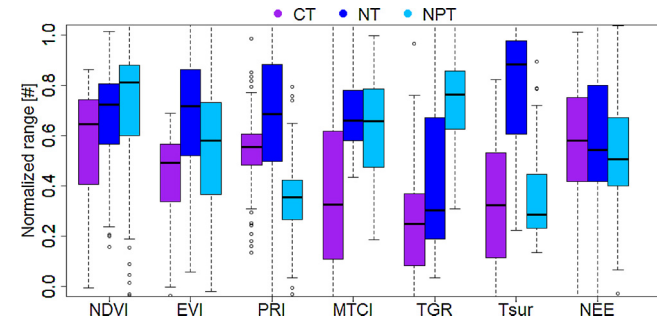
Fig. 6. Boxplots of surface properties and net ecosystem exchange (NEE) grouped by towers (purple = control tower (CT); blue = nitrogen added tower (NT); light blue = nitrogen phosphorous added tower (NPT)) and normalized by the 2.5 and 97.5th percentile of all respective values. Vegetation indexes, Tsur and NEE are calculated using footprint areas and airborne hyperspectral data for the period around the flight (April 6th – April 18th 2014) under high radiation conditions (Rg > 600 W m^{-2}). (For interpretation of the references to colour in this figure legend, the reader is referred to the web version of this article).

Fig. 7. Histograms of NEE flux uncertainties according to the random sampling error (most transparent colors and small dashed lines), the two-tower-approach (medium transparent colors and long dashed lines), and the standard deviation of the marginal distribution sampling (opaque colors and solid lines) for Spring 2014. Lines represent density fits to the respective histograms for better visibility where histograms are overlapping. CT MDS, NT MDS, and NPT MDS stand for the MDS uncertainty for the Control Tower-, Nitrogen added Tower-, and Nitrogen + Phosphorous added Tower; CT-NT TTA, NT-NPT TTA, and CT-NPT TTA for the two-tower-approach from the CT and NT tower, NT and NPT tower, and CT and NPT; and CT RE, NT RE, and NPT RE for the random sampling error of the respective towers.

of Hsieh et al., (2000), with the lateral dispersion term according to Detto et al., (2006). Input parameters for the footprint model were retrieved from EC measurements and canopy properties. Footprints were only calculated for situations under which the friction velocity was equal to or larger than the u*-threshold to ensure that a meaningful turbulent transport was present.

The roughness length (z$_0$) and displacement height (d) were estimated for individual 30° wind sectors using an optimization procedure on Eq. (1) where U is the horizontal wind speed, k the von Karman constant (0.4), and z the measurement height. Eq. (1) is valid for neutral conditions, therefore the estimations of z$_0$ and d were based on a subset of a full year including 5086 half hourly files for which z/L ranged from -0.25 to 0.25 and u* was larger 0.2 m s^{-1}. The optimization was based on a Markov Chain Monte Carlo (MCMC) algorithm using a delayed rejection and adaptive Metropolis procedure (Haario et al., 2006) as is implemented in the FME package for R.

$$U = \frac{u*}{k}\ln\left(\frac{z-d}{z_0}\right) \tag{1}$$

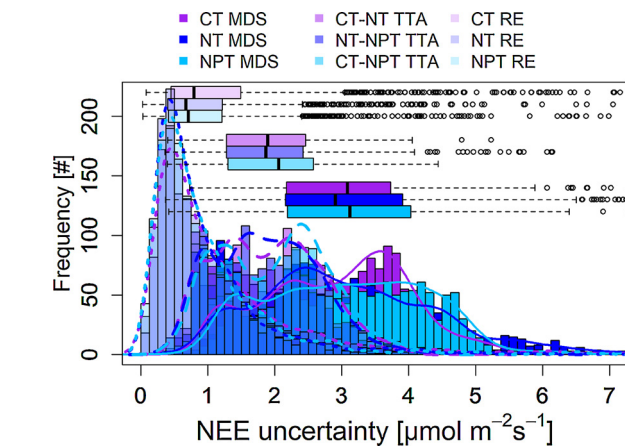### 2.4.2. Analysis of footprint area characteristics

The weighting of VIs and the extraction of the main structural properties of the ecosystem (e.g. tree, grass, and bare soil area) were done according to the footprint probability density function (PDF), by first normalizing the PDF by its integral and then multiplying each image pixel by its corresponding normalized PDF footprint weight.

As described in Section 3.1 (Spring Meteorology), a period with constant meteorological condition, 13 days around the hyperspectral flight (April 6th – April 18th), was selected to compare simultaneous between-tower flux differences (δNEE, δH, δLE calculated as e.g. NEE$_{Tower\_A}$ - NEE$_{Tower\_B}$ on half hourly scale) with the corresponding mean weighted VI (δVI calculated as VI$_{Tower\_A}$ - VI$_{Tower\_B}$) for individual half hourly footprints. To ensure that the data from the hyperspectral flight could be extrapolated to a larger time window, only high radiation data (Rg > 600 W m^{-2}) from when the flight was conducted were used. By using flux- and VI-differences for simultaneous half-hourly measurements the influence of all meteorological parameters (e.g. Rg, VPD), for flux differences, can be considered as negligible. Therefore, observed differences in flux measurements can be attributed to spatial variability in surface properties.
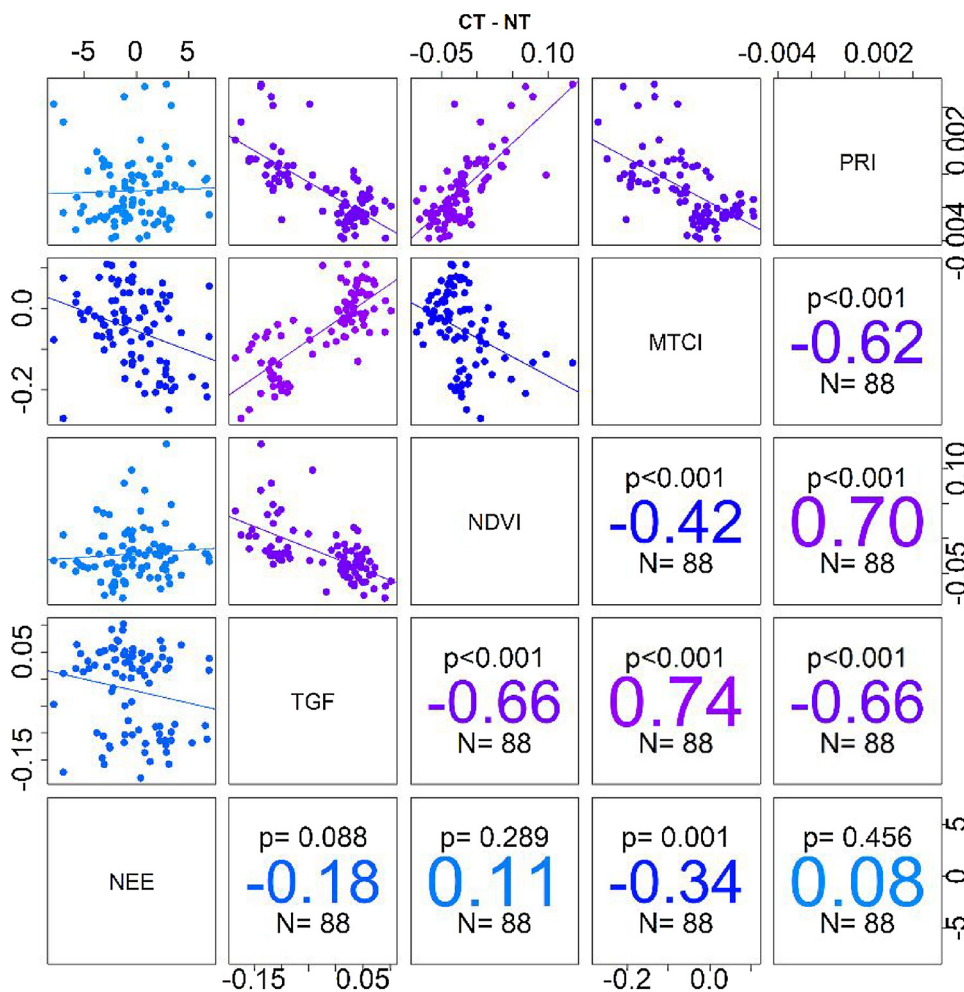
To analyze the variability of surface properties and to account for their different variability, each half hourly footprint weighted VI (VI$_i$) and other surface properties were normalized by

$$\frac{VI_i - VI_{min}}{VI_{max} - VI_{min}} \tag{2}$$

where VI$_{max}$ is the 97.5th and VI$_{min}$ the 2.5th percentile of each VI for all tower footprints.

Fig. 8. Correlation matrix of δNEE [μmol m^{-2} s^{-1}] and δVIs for CT and NT for the 13 days around the flight under high radiation conditions. Upper left boxes display the scatterplots and a linear least square fit of the respective variables. Lower right boxes show the significance level (p), the spearman correlation coefficient (colored in the center) and the number of samples (N). The diagonal boxes show the respective variables. Colors indicate the strength of the correlation. Light blue for low correlation coefficients and bright pink for high correlation coefficients. (For interpretation of the references to colour in this figure legend, the reader is referred to the web version of this article).

Two tests were performed to estimate the robustness of the results; (i) a shorter period of ± 2 days from the flight (April 6th – April 10th) was used to perform the same analysis and evaluate if, and how the results are consistent, despite meteorological and potentially biophysical changes in different time windows; (ii) the size of the footprints was changed from 90% of the PDF to 75% to evaluate how a smaller footprint size influences the analysis.

2.5. Statistical analysis

All statistical analyses were performed with R 3.2.2 (R Development Core Team, 2015). Regression analysis of half hourly flux measurements between towers was done with a major axis regression (MAR) (lmodel2 package), since it can be assumed that the variance of the errors is equal between the x- and y-variable (individual towers) (Legendre and Legendre, 1998). Regression analysis of tower differences and VI differences were performed with ordinary least square regressions, and Spearman's correlation coefficients were used. Whenever medians were compared for statistical differences the Wilcoxon-Test (for two-sample-test) or Kruskal-Wallis-Test (for three or more-samples) was used.

To identify which set of variables (meteorological variables, VI or Tsur) best explained the variability of fluxes and flux differences between towers, a multiple linear model selection algorithm (*regsubsets* from leaps-package) based on a branch-and-bound algorithm was used. NEE, H, and LE were used as the response variables and Rg, VPD, NDVI, EVI, MTCI, PRI, TGR, and Tsur as explanatory variables. The 'best' model was selected according to the lowest Bayesian Information Criterion (BIC) value to balance between performance and complexity.

In order to find the simplest model with the best performance, the BIC was used instead of the Akaike Information Criterion (AIC) to penalize more complex models stronger. Moreover, as variable selection method the relative importance analysis was also carried out using the relaimpo package (Grömping, 2006) with the Lindeman, Merenda and Gold (lmg) method. The contribution of each explanatory variable to the total R^2 is (i) calculated as the average over different orderings of explanatory variables within a respective model; (ii) step one is performed for models with different numbers of explanatory variables; (iii) the average contribution of an explanatory variable to the total R^2 is then the average of all contributions in models of different lengths.

3. Results

3.1. Spring meteorology

The most productive period of the year for the studied ecosystem typically occurs during spring, when fairly high SWC (> 20%) conditions coincide with high radiation levels and mild temperatures (Figs. 2 and A14). Especially when the herbaceous layer was growing during this time of the year. The length of the growing period was mainly driven by the amount and timing of precipitation events. The spring of 2014 started with rather low Tair around 10 °C, high SWC, low VPD, low Rg, and low GPP. This period was followed by a mild period (April 6 to April 18) with stable meteorological conditions (Tair around 20 °C, high Rg, decreasing but still relatively high SWC), during which GPP was high (mean daily value around 9 μmol m^{-2} s^{-1}) and stable (Fig. 2G). This period corresponds to the peak of productivity in terms of GPP for the year 2014. After April 18th Tair, VPD, and, Rg decrease
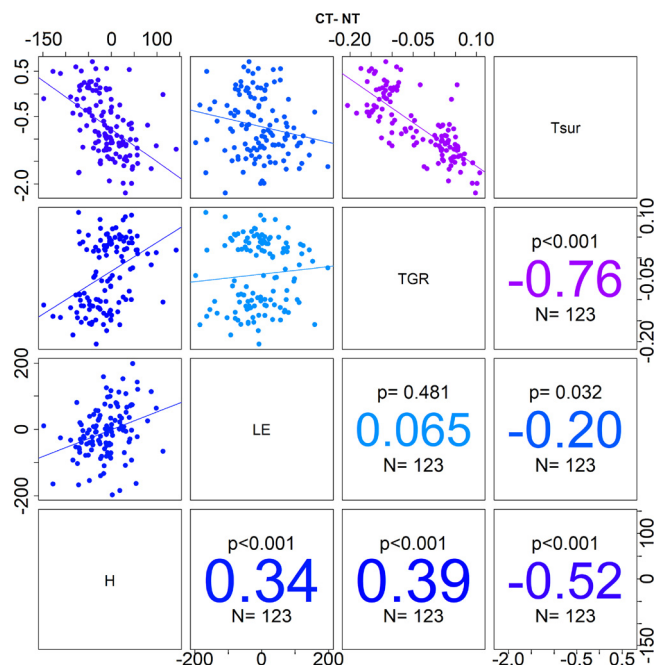
Fig. 9. Correlation matrix of δH [W m⁻²], δLE [W m⁻²], δTGR, and δTsur for NT and NPT for the period of 13 days around the flight under high radiation condition. Upper left boxes display the scatterplots and a linear least square fit of the respective variables. Lower right boxes show the significance level (p), the spearman correlation coefficient (colored in the center) and the number of samples (N). The diagonal boxes show the respective variables. Colors indicate the strength of the correlation. Light blue for low correlation coefficients and bright pink for high correlation coefficients. (For interpretation of the references to colour in this figure legend, the reader is referred to the web version of this article).

and roughly 10 mm of precipitation fell within a week. This was the last rain event before May 20th and before then both SWC and GPP were constantly decreasing, while Tair and VPD were increasing and the senescence of the herbaceous layer started. The period between the 6th and 18th of April was therefore used for a further detailed analysis in conjunction with data from the hyperspectral flight (April 8th), since the meteorological and biophysical properties of the vegetation were assumed to be constant during this period (Fig. 2 thin, vertical red lines).

3.2. Site comparison

3.2.1. Footprint composition

For a period of one year contributions of grass-, tree-, and bare soil to the flux footprints were analyzed to understand if systematic differences of the surface composition are present between the towers, using day- and nighttime data. The distribution of the footprint sizes were very similar between the sites (Fig. 3), with an inter-quartile-range of 7.5 ha (10–17.5 ha) and a median of 12.5 ha. The analysis revealed that the source areas of the EC measurements were generally similar for the three towers. In most cases the grass fraction ranged between 75 and 80% while the tree-canopy fraction ranged from 15 to 20% and the bare soil fraction accounted for less than ~5%. The sampled grass- and tree-canopy fractions at the NT showed a larger variability and the NPT usually sampled ~5–7 % more tree-canopy fraction as compared to the other towers. When only analyzing the short period around the hyperspectral flight (April 6th – April 18th 2014) under high radiation conditions (Rg > 600 W m⁻²), tree- and grass fractions were very similar to the full year but with more variability between towers (Fig. A1). Due to high Rg, atmospheric stratification was very unstable and therefore, footprints were smaller and less integrative, which caused the larger variability between towers.

3.2.2. Flux comparison

NEE, LE, H, and u* of the three towers were very similar. Figs. 4 & A2–A4 show the mean diurnal courses, standard deviations, as well as between-tower correlations for the respective variables. The data used for the mean diurnal courses are from March 25th to May 15th 2014, which represent the core of the growing season at the site. Small differences can be observed between the mean diurnal courses of the individual towers, which are smaller than the uncertainties associated to the fluxes (Sec. 3.3). Mean absolute differences of mean diurnal cycles between towers are 0.73 [μmol m⁻² s⁻¹], 4.06 [W m⁻²], 4.77 [W m⁻²], and 0.02 [m s⁻¹] for NEE, LE, H, and u*, respectively. At the CT, NEE was slightly less negative during daytime, while u* was slightly lower before noon and in the evening as compared to NT and NPT. During nighttime NEE was higher (but not significant) at the NPT as compared to CT and NT. Besides that, flux magnitudes, patterns, and their standard deviations were similar, and fluxes of LE and H agreed very well between the towers (Fig. 4). LE was larger than sensible heat fluxes and emphasizes that water was not limited during the spring period.

The MAR analysis between the towers (Fig. 5) indicated that NEE was very similar between towers during the spring of 2014. The slopes estimated from the MAR varied between 1.01 and 1.05 (corresponding to 1–5 % flux differences) and the intercept ranged from −0.31 – 0.25 μmol m⁻² s⁻¹. The best agreement was observed between NT and NPT with a slope of 1.01, an intercept of 0.25, and an r² of 0.86. Similarly results were found for H (maximum differences of 4%) and LE (maximum differences of 6%) between the towers (Figs. A2 and A3). For u* the NT and NPT were showing higher values than the CT (Figs. 4 & A4). Half hourly values of u* were 7–8 % higher, slopes of 1.07 and 1.08 for NT and ST, respectively. From the mean diurnal course of u* it seems that this underestimation was associated to the period before noon. The r² of u* are higher for all tower combinations, as compared to the other fluxes, ranging between 0.90 and 0.91. The means and standard deviations of fluxes and u* binned according to each 2.5th flux percentile of the x-value, (Figs. 5 (NEE) and A2–A4 (H, LE, u*) black circles and vertical lines) show that fluxes of NEE, LE, and H deviated more from the 1:1 line when fluxes were larger.

3.2.3. Between-site surface properties

For NDVI, EVI, PRI, and the TGR all median values of the towers were significantly different from each other (Fig. 6; p < 0.01), while for MTCI and Tsur, two towers had the same median. Relative differences of PRI were large, but absolute differences between PRI values were very small between all towers (Table 1), and suggest only little spatial variability within the footprint areas of the towers. The inner quartile range (IQR) of NDVI was very similar for the three towers but the median NDVI was increasing from CT (0.66) over NT (0.67) to NPT (0.68), even though the increase in absolute numbers was quite small. Tsur was largest at NT where the median Tsur was nearly 1 K higher as compared to the other two towers. Median Tsur was almost identical for CT and NPT (Wilcoxon-Mann-Withney Test p > 0.1) with the only difference being that at NPT the IQR was 0.3 K smaller. The distribution of the TGR within the footprints indicated lowest and highest median TGR for CT and NPT, respectively. NT was in between with a large IQR compared to the other two towers. The median values ranged between 0.2 and 0.3 for the TGR. According to the Kruskal-Wallis test, differences in NEE are not significant (p > 0.1) between towers and the Wilcoxon test shows no significant differences between the individual tower combinations (p > 0.05).

3.3. Flux uncertainty analysis

The flux uncertainty estimates (MDS, TTA, RE) exhibited distinct distributions, which reflect the different uncertainties they represent (Fig. 7). As a result, the RE showed smallest median values, which are around 0.75 μmol m⁻² s⁻¹ for NEE. For the TTA medians were roughly 2 μmol m⁻² s⁻¹ and the IQR ranged from 1.3 to 2.5 μmol m⁻² s⁻¹, while

the MDS showed medians of $3 \, \mu mol \, m^{-2} \, s^{-1}$ and IQR from 2.2 to $\sim 3.8 \, \mu mol \, m^{-2} \, s^{-1}$. The distributions of the three individual uncertainty estimates (RE, TTA, MDS) were similar between the three towers and differences between the methods were highly significant (Wilcoxon $p < 0.001$) (Fig. 7).

The three uncertainties followed similar distributions according to flux magnitudes (Fig. A13). For low fluxes the uncertainties were smallest and they increased with increasing fluxes. The MDS uncertainties were largest throughout all sampled flux magnitudes and ranged between 3 and $4 \, \mu mol \, m^{-2} \, s^{-1}$ with a relatively constant standard deviation of $2 \, \mu mol \, m^{-2} \, s^{-1}$. The mean TTA uncertainties ranged between 1.5 and $2.5 \, \mu mol \, m^{-2} \, s^{-1}$ with a standard deviation of roughly $1.5 \, \mu mol \, m^{-2} \, s^{-1}$. The mean RE was smallest (except for the largest flux bin), while its standard deviation was strongly increasing towards higher flux magnitudes. The uncertainties of MDS and TTA are not increasing as strong as RE toward higher fluxes.

The overall uncertainty estimates rank according to the various sources of flux variations that contribute to the random noise component of the signal: MDS > TTA > > RE (see also Figs. A5 & A6). The contribution of the spatial variability to the flux uncertainty is emphasized by the higher correlations between the MDS and the TTA approaches, which show substantial correlations already at daily scales ($r > 0.85$, Table A1). Generally, the correlation between approaches increases with the aggregation interval and at a scale of 8 days the difference becomes negligible.

3.4. Fluxes, vegetation indices and structural properties

For the 13 day window (April 6th – April 18th) and under high radiation conditions (consistent with CASI and AHS data acquisitions) significant correlations were found between flux differences and differences in sampled VIs (Figs. 8, 9, A7, and A8). The correlations between δNEE and δNDVI, as well as δPRI were non-significant between the towers (Fig. 8). Negative correlations between δNEE and δMTCI were significant for CT-NT, CT-NPT, but not for NT-NPT. The MTCI values between NT and NPT were more similar as compared to the CT (cf. Fig. 6 and Table 1) and δNEE between NT-NPT showed a smaller IQR as compared to the combinations with CT.

At all tower combinations δH was positively correlated with δLE and negatively correlated to δTsur. δH was further more positively correlated to the δTGR for CT-NT and NT-NPT, which were the combinations with largest differences in TGR (cf. Fig. 6 and Table 1). Additionally, at all tower combinations strong negative correlations were observed between δTsur and δTGR. Tree canopies had lower Tsur as compared to the grass layer (Fig. A9), and differences in the TGR translated into differences in Tsur. Even though δLE was positively correlated with δH no significant correlations were found between δLE, δTGR, and δTsur.

For the individual towers LE (not δLE) was significantly positive, and H significantly negatively correlated with VPD under high radiation ($Rg > 600 \, W \, m^{-2}$) conditions (Figs. A10–A12). For NT and CT significant negative correlations were observed between H and Tsur within the footprint. Additionally, Tsur was negatively correlated with the TGR, indicating lower Tsur at higher tree canopy cover within the footprints (Fig. A9). This correlation was strongest at NT and CT and both towers indicated a reduction in average footprint Tsur of roughly 0.7 K per 0.1 increases in TGR. This ratio can be observed for tower differences and at individual towers (Figs. 9, A10 and A11).

The multiple linear model selection based on BIC showed for NEE at each individual tower that VPD is the strongest explanatory variable. While, the model selection for the flux differences between two towers selected 1 or 2 variables, which were MTCI (for CT/NT and CT/NPT) and NDVI and EVI (for NT/NPT).

The method validation proved the robustness of merging VI-maps with results from the footprint analysis against uncertainties in the selected footprint size (90%) and window width (13 days). Reducing

the time window for the analysis increased the correlation coefficients between δMTCI and δNEE from -0.34 to -0.65 for the differences between CT and NT, and from -0.29 to -0.39 for CT and NPT. This indicated that the temporal extrapolation of the MTCI introduced additional uncertainties to the analysis, but increases the number of samples that can be used for the analysis. For δTsur and δH the correlation coefficient increased with the shorter time window by 0.09 (CT/NT), 0.04 (CT/NPT), and 0.09 (NT/NPT). The reduction of footprint size resulted in nearly no change to the correlations because, (i) the weighing of the VI-values by the PDF of the footprint accounted already for the contribution to the flux which was largely captured by the 75% footprint, even though the area of the 90% footprint was much larger and (ii) the footprint areas at each tower were homogeneous with no major changes in vegetation or other surface properties.

4. Discussion

The results of the turbulent flux comparison during spring 2014 demonstrate that the three eddy covariance towers and located within a homogenous landscape (at footprint scale i.e. several ha) used in this analysis, are measuring on average similar fluxes at half-hourly and daily time scales (Fig. 4). Half hourly flux measurements correlate very good between the three towers, and show better or similar agreements than values reported in the literature for similar comparisons (Eugster et al., 1997; Hollinger et al., 2004; Rannik et al., 2006). However, individual half hourly fluxes can vary strongly, especially for large fluxes (Figs. 5; A2–A4). These differences are attributed to random uncertainties associated to the eddy covariance technique (Richardson et al., 2012), but can be partly attributed to spatial heterogeneity, as shown above. Several studies (e.g. Hollinger and Richardson, 2005; Lasslop et al., 2008) showed the increase of the random uncertainty with the flux magnitude independent of the method used (Fig. A13), which is in line with the observations of larger scatter when comparing two towers (Figs. 5; A2–A4). In this analysis, the uncertainties of the MDS and the TTA increase from smaller to larger fluxes and flattened out toward the most negative NEE values, while the RE increased linearly. As the TTA approach is based on differences between flux tower measurements, it includes spatial heterogeneity in its flux uncertainty estimate. Therefore, it characterizes not only the random uncertainty of flux measurements but also the uncertainty associated to spatial heterogeneity. In our case the uncertainty associated to spatial heterogeneity of the flux measurements would be 2–3 times larger as the RE when comparing their medians (Fig. 7). We emphasize that the distributions and medians of the three uncertainty estimates were significantly different from each other, but similar between the towers (Fig. 7). This means that not only fluxes, but also the associated flux uncertainties are similar within a homogeneous ecosystem. The differences between the methods suggest that the uncertainty estimates were a result of a random flux component as well as spatial heterogeneity, temporal variability, and small meteorological variability. In the following we will discuss potential causes and implications for the different uncertainty magnitudes of three applied methods.

Spatial variability in fluxes (which increases the uncertainty estimate from the MDS and TTA) can arise from variability in vegetation properties and composition, changes in soil properties e.g. nutrient and water availability, topography, or stand age. Different magnitudes of calculated uncertainties have an impact in the propagation of flux uncertainties when calculating e.g. annual sums. But these methodological differences also translate in different correlations between the methods (Table A1). This is of interest because temporal changes in the uncertainty estimates affect the relative importance of individual observations and can propagate to ecosystem parameters in model inversion exercises (e.g. Wang et al., 2011; Williams et al., 2009).

The opportunistic situation with three EC-towers within one ecosystem allowed to evaluate whether and how the three uncertainty estimates agree at different locations within one homogeneous

ecosystem. A similar test could be performed at other ecosystems by using a mobile EC-tower which can be placed at various locations within a homogenous area. The RE and the MDS can be performed with one tower at different locations. As the magnitude of the MDS is not only depending on spatial variability but also on the variability of ecosystem processes and phenology (within the +/− 7-day window) the magnitude of the MDS might not be comparable throughout the year. In fact, only the TTA needs more than one EC-tower to be performed and this problem can be overcome. Hollinger and Richardson (2005) addressed exactly this problem and developed the successive days approach (SDA) which creates paired measurements by comparing flux measurements exactly 24 h apart from each other under similar meteorological conditions. They observed that the uncertainty of the SDA was generally greater than that of the TTA, which fits well into our findings, where the MDS uncertainty yielded larger uncertainties as the TTA. Richardson et al. (2012) stated also that the inclusion of the wind direction to the SDA reduced the uncertainty estimates, but at the cost of data loss (i.e. less 'paired' observations). We argue that the overlap of the respective footprints or surface properties within the footprints should be used for the SDA to account for spatial variability of surface properties. Comparing the average flux differences between the three towers with the estimated flux uncertainties of the RE, TTA, and MDS methods, leads to the conclusion that within a reasonably homogeneous ecosystem fluxes are spatially invariant and therefore, towers are measuring the same aggregated fluxes even though small scale spatial variability is present.

Instantaneous half-hourly flux differences between co-located towers are associated to spatial heterogeneity of biophysical properties and ecosystem structures. During the spring period, half-hourly flux differences of NEE between towers were correlated with spatial variability of MTCI (Fig. 8). The MTCI is a good proxy for canopy chlorophyll content, which is sensitive to the LAI and greenness of the vegetation, therefore it is a good proxy for the photosynthetic uptake of CO_2 by the vegetation (Dash and Curran, 2007). We showed that flux differences of NEE between the three towers (under high radiation conditions) are correlated to changes in MTCI, and therefore to changes in chlorophyll content of the canopy within the flux-footprints. Higher canopy chlorophyll content results in more carbon uptake (i.e. more negative NEE). This relationship is only visible when meteorological differences are eliminated (co-located towers), and when differences in MTCI are large enough. The range between the 10th and 90th percentile of MTCI differences between the NT and NPT is only 0.1, while it is 0.2 and 0.25 between CT and NPT/NT, respectively. Due to the minor differences between NPT and NT the signal is most likely too small and buried in the random noise of the measurements.

Half hourly between-tower differences of H were correlated to spatial variability of TGR and Tsur (Figs. 8, 9, A9). The correlation between H, Tsur, and TGR is more pronounced and visible for both, tower difference and individual towers. The sampled TGR within footprints is strongly negatively correlated to the average Tsur of the respective footprints (Fig. 9). Tree canopies have a lower aerodynamic resistance as compared to the herbaceous layer (e.g. Baldocchi and Ma, 2013), and can therefore dissipate heat more efficiently in form of additional H. In other words, tree canopies are an additional source of H and lower the average surface temperatures (Fig. A9a) within the footprints. This counter-intuitive relationship is so pronounced because trees contribute 50% of the ecosystem H during spring period (data not shown), and because biophysical differences between the herbaceous layer and the trees are large. At a homogeneous forest or grassland, H would mostly be positively correlated to Tsur during daytime conditions.

Even though δH and δLE are strongly positively correlated to each other at all tower combinations, δLE is only weakly correlated (at one tower combination CT/NT) with δTsur. The explanation for the missing correlation lies in the different contribution of the herbaceous layer and the tree canopy to LE and H, which is influenced by the iso- and anisohydricity of the trees and the herbaceous layer, respectively. *Quercus ilex* trees are rather isohydric and close their stomata when e.g. VPD is high (Garcia-Forner et al., 2016; Quero et al., 2011). The contribution of the trees to LE is therefore small, while the contribution to H is large. In contrast, the annual plants are rather anisohydric, they do not close their stomata to reduce transpiration under high VPD conditions as long as the soil water content (SWC) is high enough (Brilli et al., 2011; McDowell et al., 2008). During the analyzed period SWC was high (above 20%; Fig. 2b) and the herbaceous layer transpired as much as needed. Additionally, evaporation of soil water will increase with higher atmospheric demand, i.e. high VPD, which is emphasized by the strong positive correlation between VPD and LE (at all towers). We could not observe indications for reduced LE under high VPD conditions. The analysis of diurnal cycles of LE also did not provide evidence of hysteresis i.e. a reduction of LE in the afternoon. As a result, the herbaceous layer contributes, strongly to LE but less to H. These different contributions to LE and H by the herbaceous layer and the tree canopy offers an explanation as to why δH and δLE are corelated to each other, but only δH is correlated with δTsur.

The relationship of half hourly between-tower differences of fluxes and surface properties (i.e. canopy fraction, chlorophyll content, and surface temperature) shows how, spatial variability in biophysical properties and therefore in fluxes, can be interpreted as random uncertainty of the measurements, and that different fluxes (NEE, H, LE) might have different causes (i.e. spatial heterogeneity of MTCI, Tsur or TGR) rather than only random error.

5. Conclusions

This work explores the relationships between flux variability, spatial variability of surface properties (vegetation indices, surface temperature, and tree-grass-ratio), and how these influence uncertainty estimates within a savanna-type ecosystem. The three co-located eddy covariance towers, used in this study showed no significant differences in average fluxes of H, LE, and NEE. Therefore, these results emphasize that the eddy covariance method is able to measure the same fluxes independent of the tower location, if the surface properties are similar enough at footprint scale within a given ecosystem. The use of high resolution hyperspectral and thermal remote sensing data in combination with footprint modelling proved to be able to partly attribute half hourly flux differences to surface properties, and allowed to identify drivers of spatial heterogeneity in flux measurements. The spatial variability of canopy chlorophyll content (i.e. quantified with MTCI) and surface temperature were correlated with NEE and H, respectively. Drivers of spatial heterogeneity can vary for different fluxes and also between biophysical properties or state variables e.g. chlorophyll content, LAI, surface temperature, structure. It is important to remember, that the relationship between spatial variability of biophysical properties and flux footprint size determines if the flux variability or the flux magnitude are affected. As spatial variability in surface properties influences flux measurements it has a direct impact on commonly used uncertainty estimates like the standard deviation of the marginal distribution sampling, the successive days approach, and the two-tower-approach, by adding spatial variability into the random uncertainty estimate, and thereby overestimating the random uncertainty. However, when data of the analyzed ecosystem are aggregated at longer time scales spatial variability averages out.

We suggest that further research is needed to better understand the impact of applying different flux uncertainty estimates, and aggregations to estimate biosphere model parameters using model data integration approaches and model inversions.
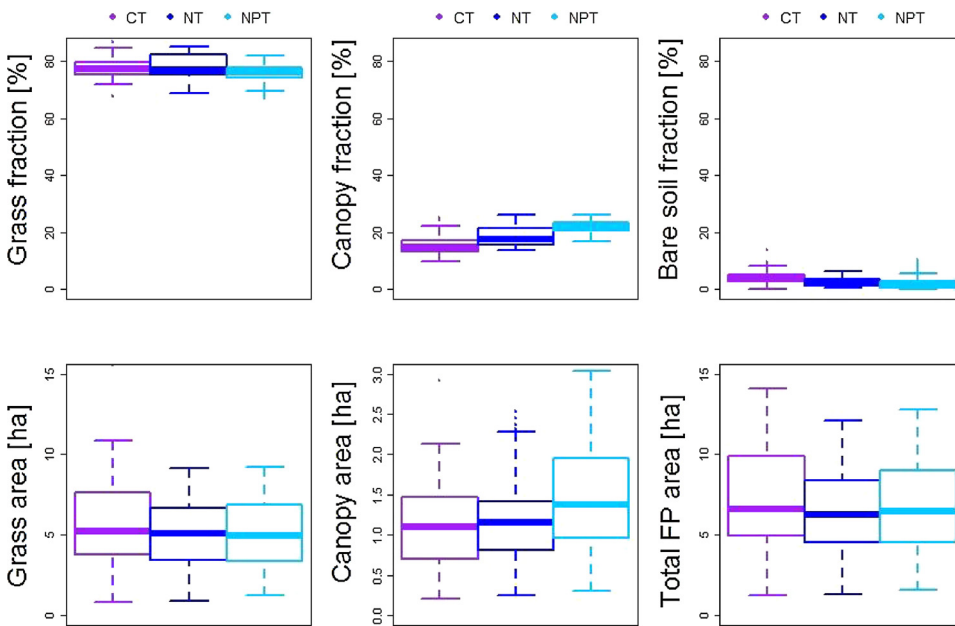
Acknowledgements

Appendix

See Figs. A5 and A6

**Fig. A1.** Boxplots of footprint characteristics for the individual towers for the period around the hyperspectral flight (April 6th – April 18th) using only daytime data with Rg > 600 W m^{-2}.
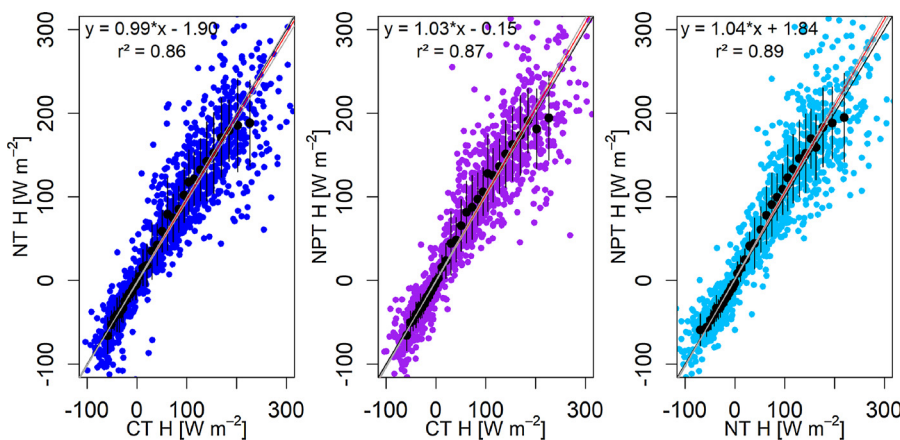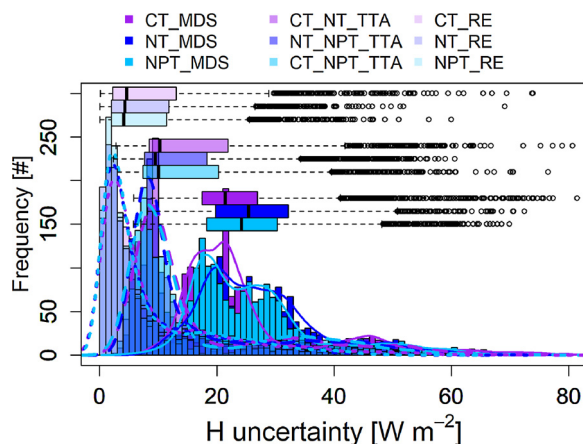

Fig. A2. Correlations of half hourly H-fluxes [W m^{-2}] between towers for spring 2014 (March 25th and May 15th 2014). Black line is 1:1 line, red line is linear fit according to the major axis regression with the respective formula and r^2 values in the upper left corner. The grey lines represent the 2.5 and 97.5% confidence intervals of the linear fit. The full black circles and vertical lines indicate the mean and standard deviation of the y-values for each 2.5th percentile of the respective x-values.
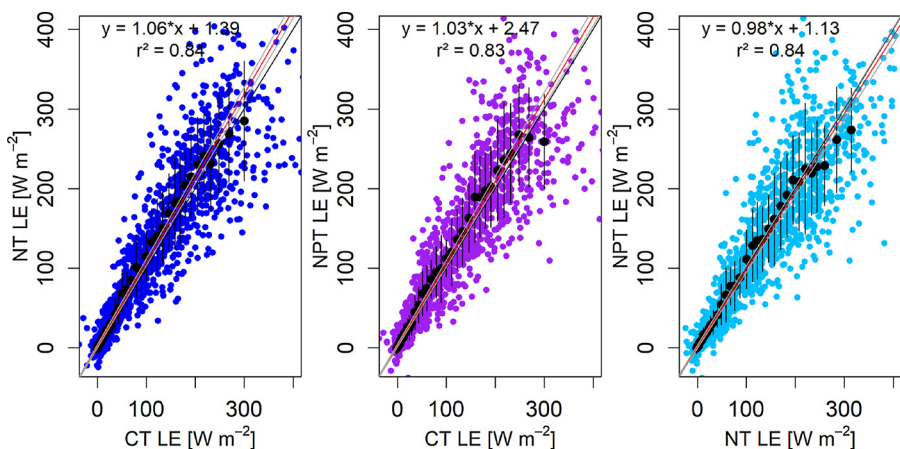
Fig. A3. Correlations of half hourly LE-fluxes [W m^{-2}] between towers for spring 2014 (March 25th and May 15th 2014). Black line is 1:1 line, red line is linear fit according to the major axis regression with the respective formula and r^2 values in the upper left corner. The grey lines represent the 2.5 and 97.5% confidence intervals of the linear fit. The full black circles and vertical lines indicate the mean and standard deviation of the y-values for each 2.5th percentile of the respective x-values.
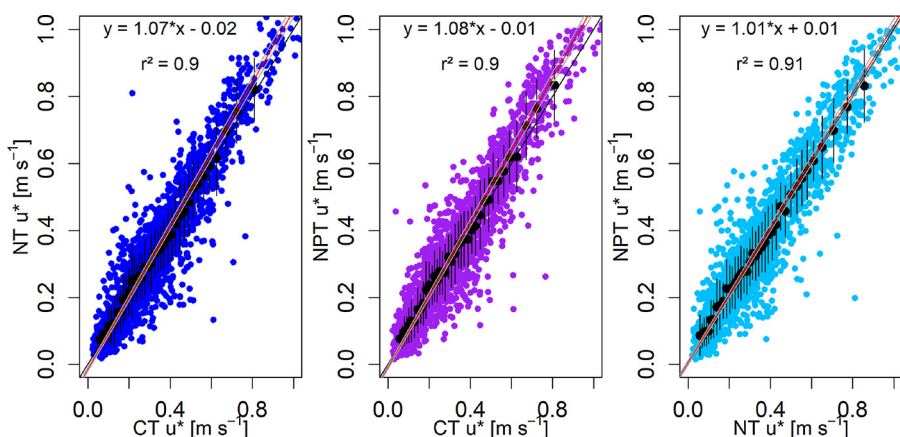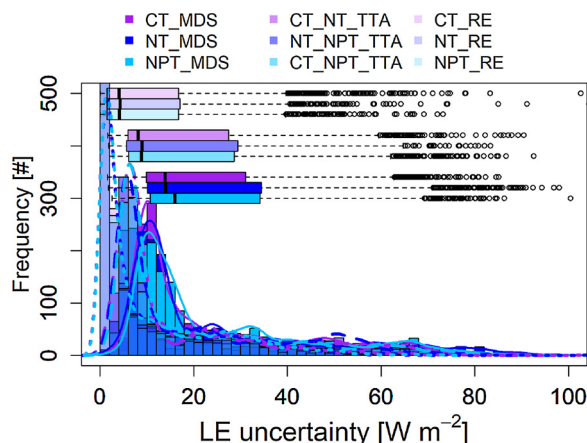

Fig. A4. correlations of half hourly u* [m s^{-1}] between towers for spring 2014 (March 25th and May 15th 2014). Black line is 1:1 line, red line is linear fit according to the major axis regression with the respective formula and r^2 values in the upper left corner. The grey lines represent the 2.5 and 97.5% confidence intervals of the linear fit. The full black circles and vertical lines indicate the mean and standard deviation of the y-values for each 2.5th percentile of the respective x-values.
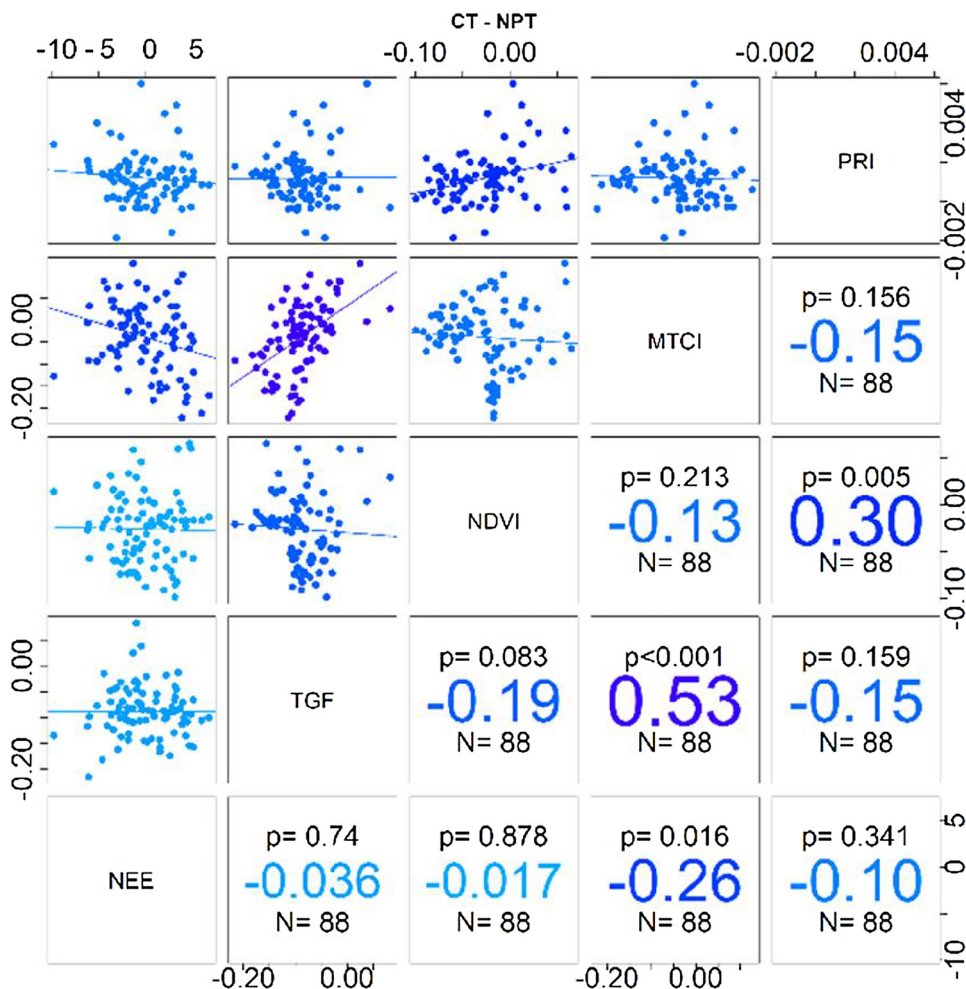

Fig. A5. Histograms of flux uncertainties according to the random sampling error (most transparent colors and small dashed lines), the two tower approach (medium transparent colors and long dashed lines), and the standard deviation of the marginal distribution sampling (opaque colors and solid lines) for Spring 2014. Lines represent density fits to the respective histograms for better visibility where histograms are overlapping. CT_MDS, NT_MDS, and NPT_MDS stand for the MDS uncertainty for the Control Tower-, Nitrogen added Tower-, and Nitrogen + Phosphorous added Tower; CT_NT_TTA, NT_NPT_TTA, and CT_NPT_TTA for the two tower approach from the CT and NT tower, NT and NPT tower, and CT and NPT; and CT_RE, NT_RE, and NPT_RE for the random sampling error of the respective towers.

Fig. A6. Histograms of flux uncertainties according to the random sampling error (most transparent colors and small dashed lines), the two tower approach (medium transparent colors and long dashed lines), and the standard deviation of the marginal distribution sampling (opaque colors and solid lines) for Spring 2014. Lines represent density fits to the respective histograms for better visibility where histograms are overlapping. CT_MDS, NT_MDS, and NPT_MDS stand for the MDS uncertainty for the Control Tower-, Nitrogen added Tower-, and Nitrogen + Phosphorous added Tower; CT_NT_TTA, NT_NPT_TTA, and CT_NPT_TTA for the two tower approach from the CT and NT tower, NT and NPT tower, and CT and NPT; and CT_RE, NT_RE, and NPT_RE for the random sampling error of the respective towers.
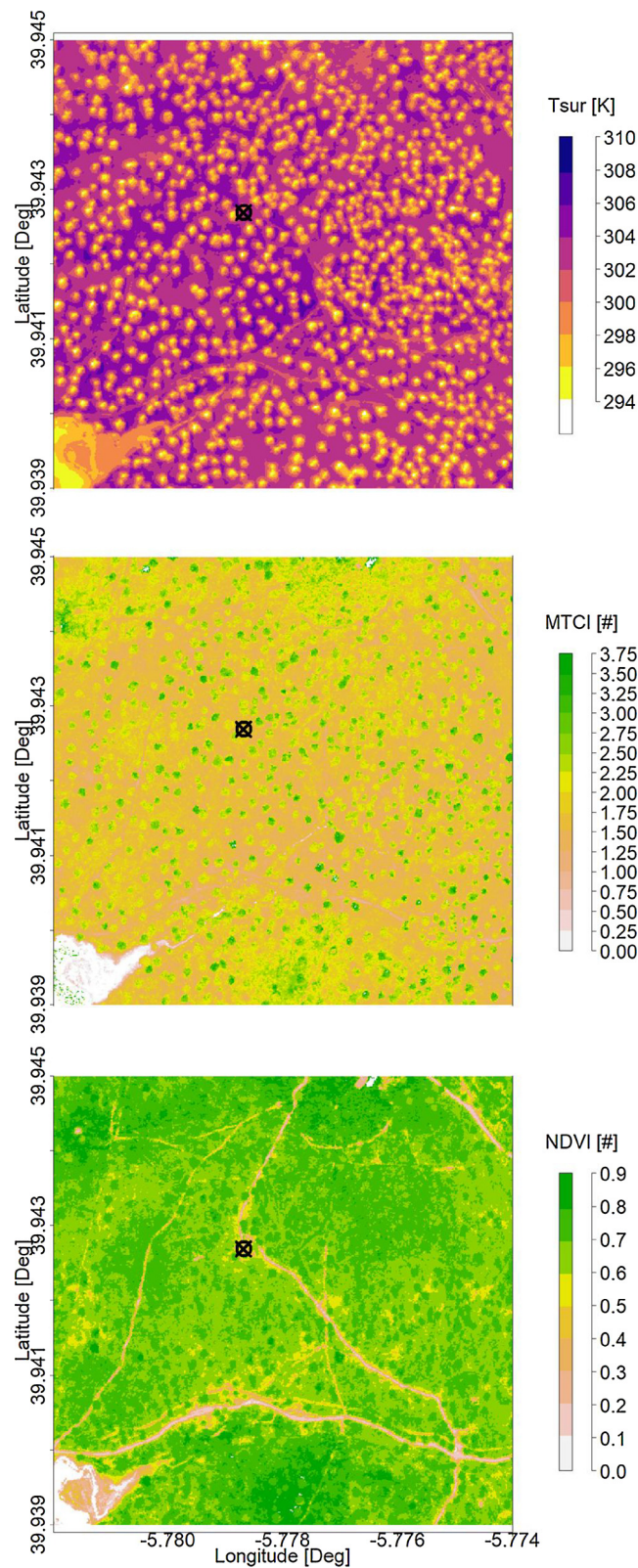

Fig. A7. Correlation matrix of δNEE and δVIs for CT and NPT for the 13 days around the flight under high radiation condition. Upper left boxes display the scatterplots and a linear least square fit of the respective variables. Lower right boxes show the significance level (p), the spearman correlation coefficient (colored in the center) and the number of samples (N). The diagonal boxes show the respective variables. Colors indicate the strength of the correlation. Light blue for low correlation coefficients and bright pink for high correlation coefficients.
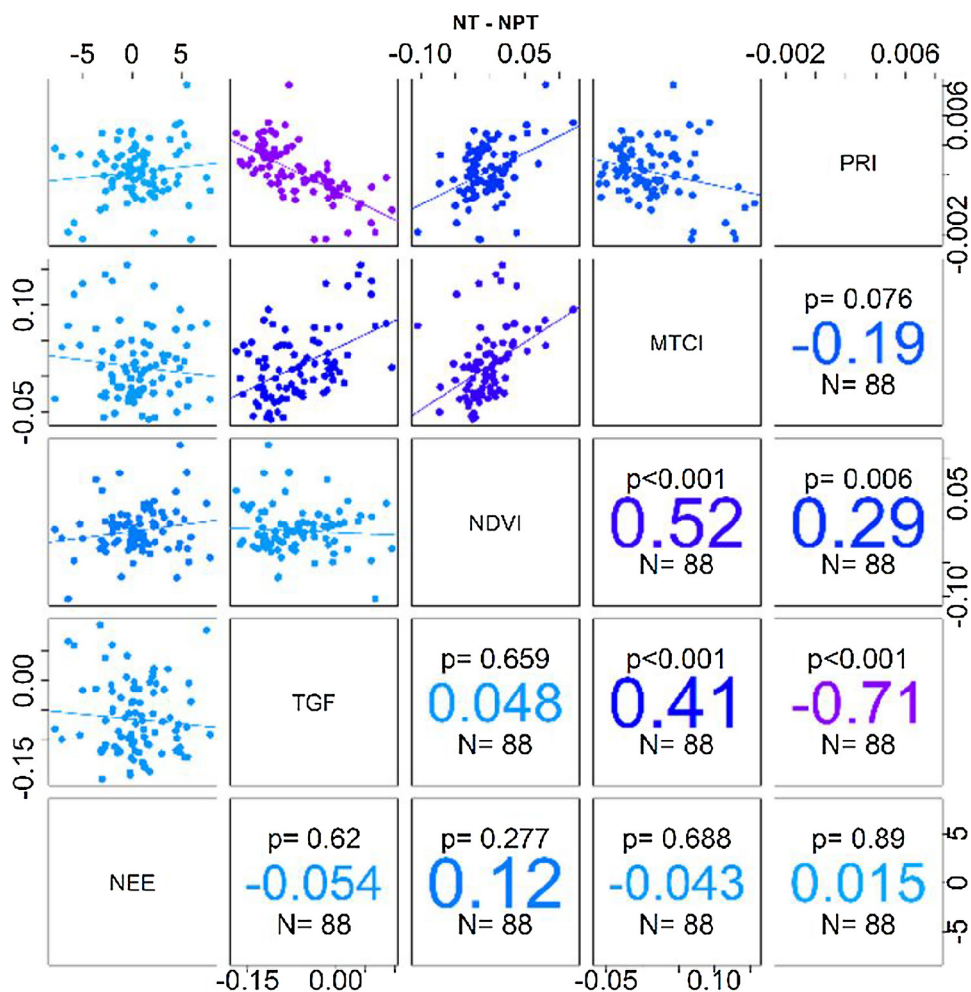
Fig. A8. Correlation matrix of δNEE and δVIs for NT and NPT for the 13 days around the flight under high radiation condition. Upper left boxes display the scatterplots and a linear least square fit of the respective variables. Lower right boxes show the significance level (p), the spearman correlation coefficient (colored in the center) and the number of samples (N). The diagonal boxes show the respective variables. Colors indicate the strength of the correlation. Light blue for low correlation coefficients and bright pink for high correlation coefficients.

Fig. A9. Surface temperatures (top), MTCI (middle) and NDVI (bottom) as measured with the airborne hyperspectral scanner on April 8th. Black circles with cross indicates the position of the nitrogen added tower. Yellow circular structures in top panel (low surface temperatures) are trees. Brownish line structures in the NDVI plot (bottom) are dirt roads and cable tranches.
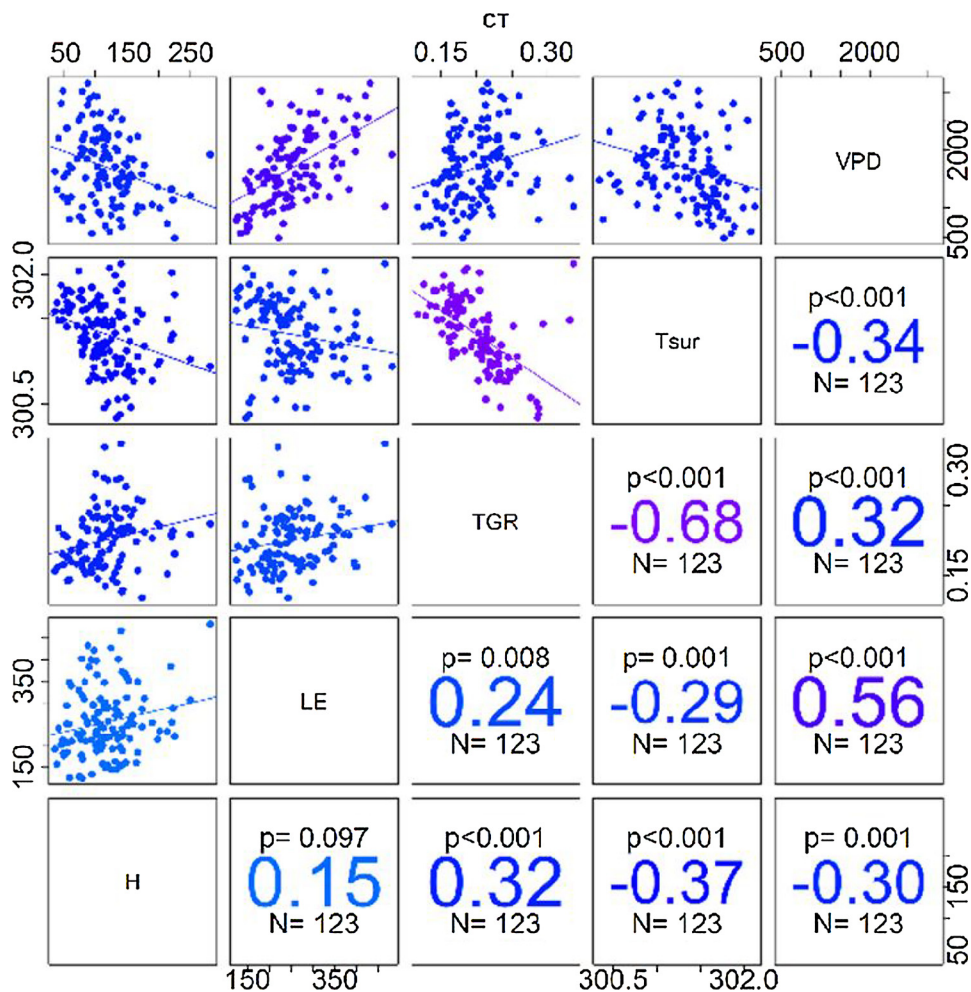
Fig. A10. Correlation matrix of H and LE of the CT with tree-grass-ratio (TGR), surface temperature (Tsur), and vapor pressure deficit (VPD) for the 13 days around the flight under high radiation condition. Upper left boxes display the scatterplots and a linear least square fit of the respective variables. Lower right boxes show the significance level (p), the spearman correlation coefficient (colored in the center) and the number of samples (N). The diagonal boxes show the respective variables. Colors indicate the strength of the correlation. Light blue for low correlation coefficients and bright pink for high correlation coefficients.
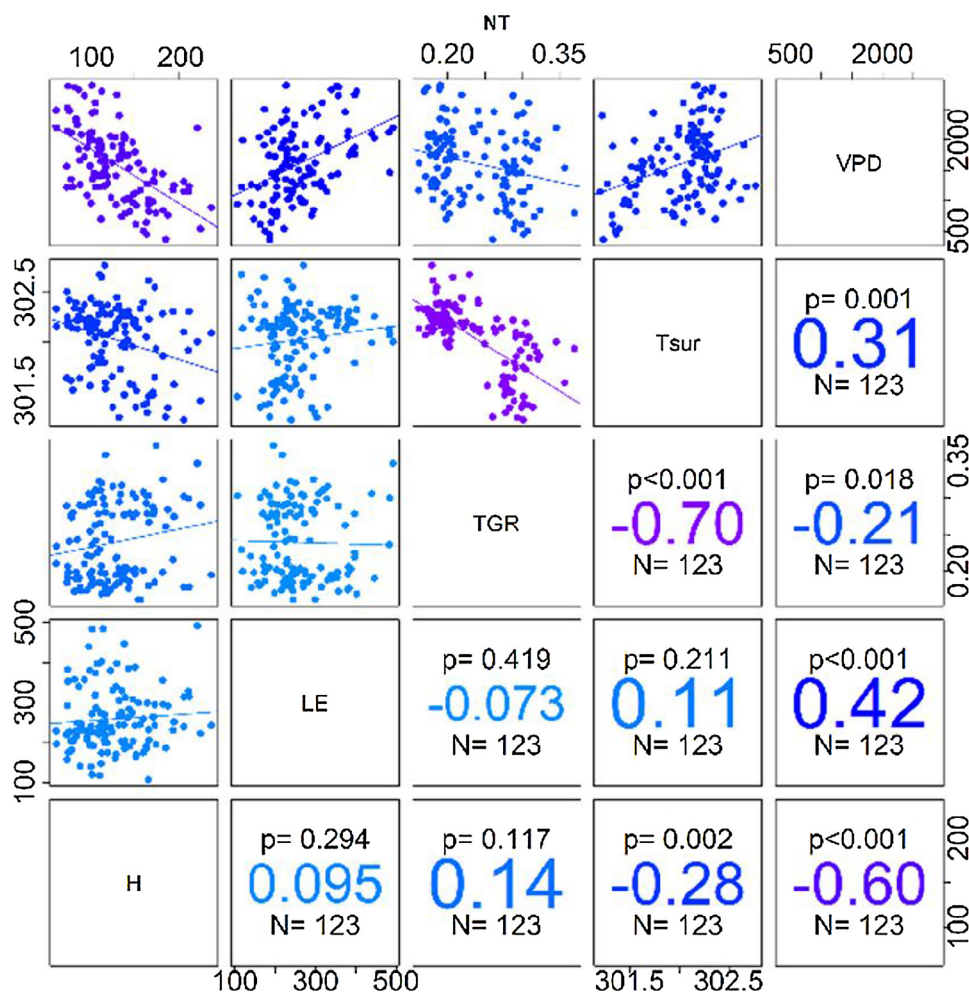
Fig. A11. Correlation matrix of H and LE of the NT with tree-grass-ratio (TGR), surface temperature (Tsur), and vapour pressure deficite (VPD) for the 13 days around the flight under high radiation condition. Upper left boxes display the scatterplots and a linear least square fit of the respective variables. Lower right boxes show the significance level (p), the spearman correlation coefficient (colored in the center) and the number of samples (N). The diagonal boxes show the respective variables. Colors indicate the strength of the correlation. Light blue for low correlation coefficients and bright pink for high correlation coefficients.
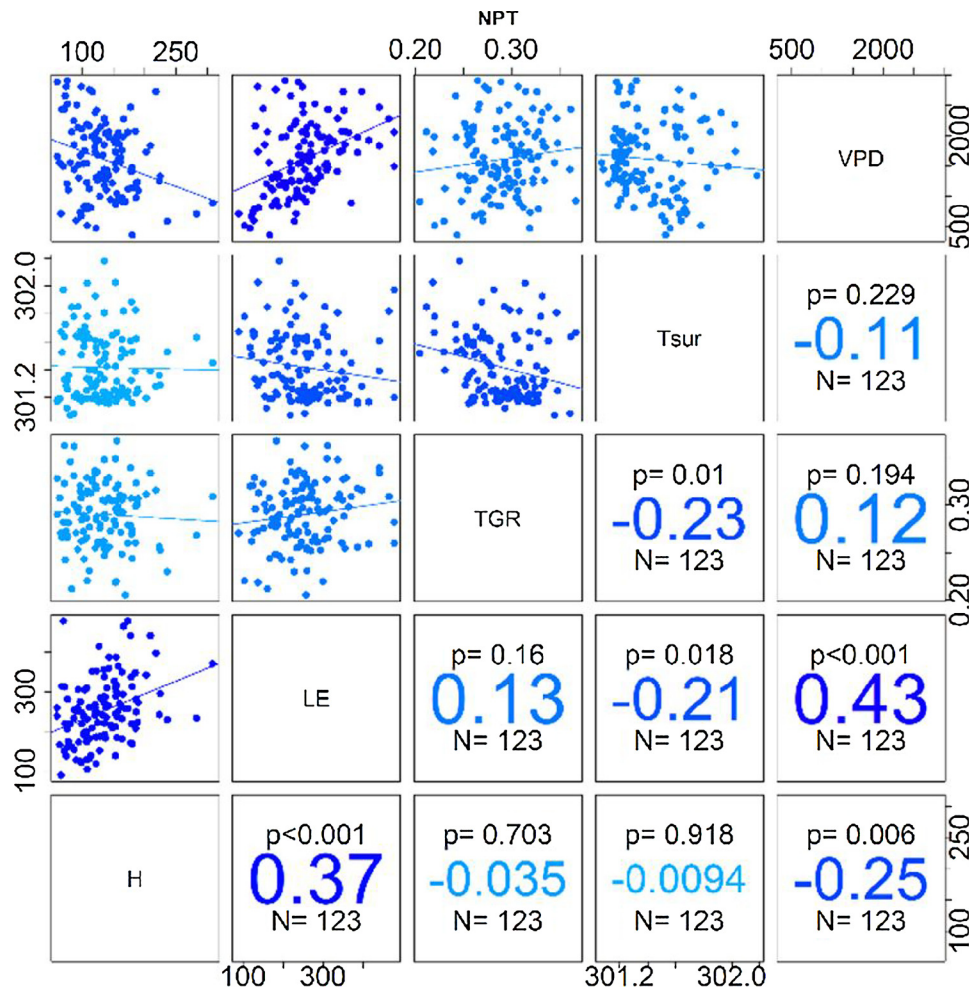
Fig. A12. Correlation matrix of H and LE of the NPT with tree-grass-ratio (TGR), surface temperature (Tsur), and vapour pressure deficite (VPD) for the 13 days around the flight under high radiation condition. Upper left boxes display the scatterplots and a linear least square fit of the respective variables. Lower right boxes show the significance level (p), the spearman correlation coefficient (colored in the center) and the number of samples (N). The diagonal boxes show the respective variables. Colors indicate the strength of the correlation. Light blue for low correlation coefficients and bright pink for high correlation coefficients.
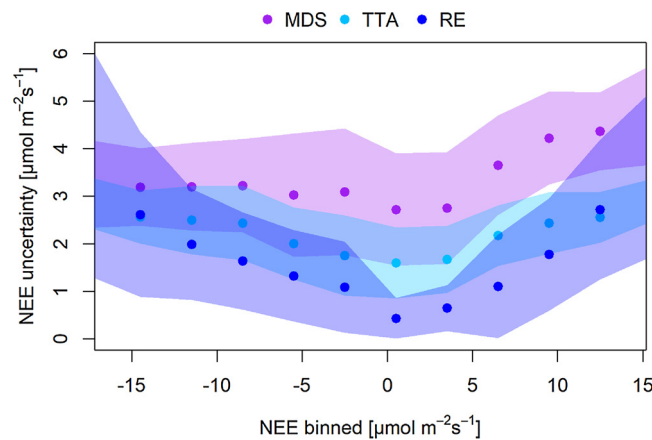

Fig. A13. Mean flux uncertainty binned according to flux magnitude of NEE for spring 2014. Filled circles represent the mean flux uncertainty for a flux bin and the three towers (CT,NT,NPT) from the MDS approach (purple), the two tower approach (light blue), and the random error (blue). Shaded areas correspond to the standard deviations from the binning.
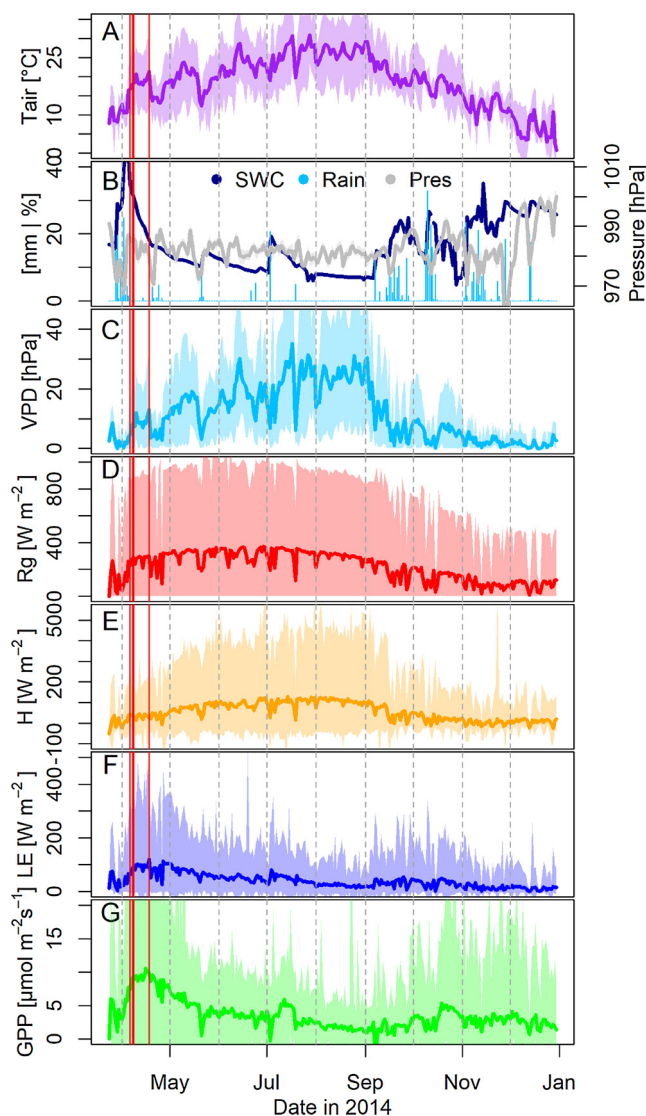
Fig. A14. Time-series from March 25th 2014 – January 1st 2015 of mean daily air temperature (°C) at 2 m above ground (A), volumetric soil water content (%) in 10 cm depth as well as daily sums of precipitation (mm) (B), vapor pressure deficit (VPD; hPa) calculated from temperature and relative humidity at 2 m above ground level (C), global radiation (Rg; W m^{-2}) (D), sensible heat flux (H; W m^{-2}) (E), latent heat flux (LE; W m^{-2}) (F), and gross primary productivity (GPP; μmol m^{-2} s-1) (G) as measured at the nitrogen added tower. Solid lines are daily averages and shaded areas the respective minimum and maximum values calculated for each day. The thin vertical red lines mark the period around the flight (April 6th – April 18th) which was used for additional analysis; the bold red line indicates the flight day (April 8th). Grey dashed lines represent the first day of each month.

Table A1
Pearson correlation coefficient between different uncertainty estimates for 30 min, 1 day, and 8 day aggregation periods.

Tower / Average Period	Methods	30 Min	1 Day	8 Day
CT	MDS/RE	0.29	0.24	0.68
	MDS/TTA	0.73	0.88	0.93
	RE/TTA	0.37	0.39	0.86
NT	MDS/RE	0.28	0.38	0.95
	MDS/TTA	0.73	0.90	0.98
	RE/TTA	0.36	0.41	0.95
NPT	MDS/RE	0.29	0.57	0.97
	MDS/TTA	0.75	0.94	0.98
	RE/TTA	0.41	0.57	0.92

References

Ahlstrom, A., Raupach, M.R., Schurgers, G., Smith, B., Arneth, A., Jung, M., Reichstein, M., Canadell, J.G., Friedlingstein, P., Jain, A.K., Kato, E., Poulter, B., Sitch, S., Stocker, B.D., Viovy, N., Wang, Y.P., Wiltshire, A., Zaehle, S., Zeng, N., 2015. The dominant role of semi-arid ecosystems in the trend and variability of the land CO2 sink. Science 348, 895–899. https://doi.org/10.1126/science.aaa1668.

Aubinet, M., Chermanne, B., Vandenhaute, M., Longdoz, B., Yernaux, M., Laitat, E., 2001. Long term carbon dioxide exchange above a mixed forest in the Belgian Ardennes. Agric. For. Meteorol. 108, 293–315.

Baldocchi, D., Ma, S., 2013. How Will Land Use Affect Air Temperature in the Surface Boundary Layer? Lessons Learned from a Comparative Study on the Energy Balance of an Oak Savanna and Annual Grassland in California. Tellus B 65, USA. https://doi.org/10.3402/tellusb.v65i0.19994.

Balzarolo, M., Vescovo, L., Hammerle, A., Gianelle, D., Papale, D., Tomelleri, E., Wohlfahrt, G., 2015. On the relationship between ecosystem-scale hyperspectral reflectance and CO&sub2&/sub& exchange in European mountain grasslands. Biogeosciences 12, 3089–3108. https://doi.org/10.5194/bg-12-3089-2015.

Brilli, F., Hörtnagl, L., Hammerle, A., Haslwanter, A., Hansel, A., Loreto, F., Wohlfahrt, G., 2011. Leaf and ecosystem response to soil water availability in mountain grasslands. Agric. For. Meteorol. 151, 1731–1740. https://doi.org/10.1016/j.agrformet.2011.07.007.

Casals, P., Gimeno, C., Carrara, A., Lopez-Sangil, L., Sanz, Mj., 2009. Soil CO2 efflux and extractable organic carbon fractions under simulated precipitation events in a Mediterranean Dehesa. Soil Biol. Biochem. 41, 1915–1922. https://doi.org/10.1016/j.soilbio.2009.06.015.

Chen, C., Cleverly, J., Zhang, L., Yu, Q., Eamus, D., 2016. Modelling seasonal and interannual variations in carbon and water fluxes in an Arid-Zone Acacia Savanna Woodland, 1981–2012. Ecosystems 19, 625–644. https://doi.org/10.1007/s10021-015-9956-8.

Costa-e-Silva, F., Correia, A.C., Piayda, A., Dubbert, M., Rebmann, C., Cuntz, M., Werner, C., David, J.S., Pereira, J.S., 2015. Effects of an extremely dry winter on net ecosystem carbon exchange and tree phenology at a cork oak woodland. Agric. For. Meteorol. 204, 48–57. https://doi.org/10.1016/j.agrformet.2015.01.017.

Dash, J., Curran, P.J., 2004. The MERIS terrestrial chlorophyll index. Int. J. Remote Sens. 25, 5403–5413. https://doi.org/10.1080/0143116042000274015.

Dash, J., Curran, P.J., 2007. Evaluation of the MERIS terrestrial chlorophyll index (MTCI). Adv. Space Res. 39, 100–104. https://doi.org/10.1016/j.asr.2006.02.034.

Detto, M., Montaldo, N., Albertson, J.D., Mancini, M., Katul, G., 2006. Soil moisture and vegetation controls on evapotranspiration in a heterogeneous Mediterranean ecosystem on Sardinia, Italy: evapotranspiration in Mediterranean ecosystem. Water Resour. Res. 42https://doi.org/10.1029/2005WR004693. n/a-n/a.

Dubbert, M., Piayda, A., Cuntz, M., Correia, A.C., Costa e Silva, F., Pereira, J.S., Werner, C., 2014. Stable oxygen isotope and flux partitioning demonstrates understory of an oak savanna contributes up to half of ecosystem carbon and water exchange. Front. Plant Sci. 5. https://doi.org/10.3389/fpls.2014.00530.

Eamus, D., Cleverly, J., Boulain, N., Grant, N., Faux, R., Villalobos-Vega, R., 2013. Carbon and water fluxes in an arid-zone Acacia Savanna Woodland: an analyses of seasonal patterns and responses to rainfall events. Agric. For. Meteorol. 182–183, 225–238. https://doi.org/10.1016/j.agrformet.2013.04.020.

Eugster, W., McFadden, J.P., Chapin, F.S., 1997. A comparative approach to regional variation in surface fluxes using mobile eddy correlation towers. Boundary Layer Meteorol. 85, 293–307.

Finkelstein, P.L., Sims, P.F., 2001. Sampling error in eddy correlation flux measurements. J. Geophys. Res. Atmos. 106, 3503–3509. https://doi.org/10.1029/2000jd900731.

Fratini, G., Mauder, M., 2014. Towards a consistent eddy-covariance processing: an intercomparison of EddyPro and TK3. Atmos. Meas. Tech. 7, 2273–2281. https://doi.org/10.5194/amt-7-2273-2014.

Gamon, J.A., Penuelas, J., Field, C.B., 1992. A narrow-waveband spectral index that tracks diurnal changes in photosynthetic efficiency. Remote Sens. Environ. 41, 35–44.

Gao, F., Kustas, W., Anderson, M., 2012. A data mining approach for sharpening thermal satellite imagery over land. Remote Sens. 4, 3287–3319. https://doi.org/10.3390/rs4113287.

Garcia-Forner, N., Beil, C., Save, R., Martinez-Vilalta, 2016. Isohydric species are not necessarily more carbon limited than anisohydric species during drought. Tree Physiol. https://doi.org/10.1093/treephys/tpw109.

Gillespie, A., Rokugawa, S., Matsunaga, T., Cothern, J.S., Hook, S., Kahle, A.B., 1998. A temperature and emissivity separation algorithm for advanced spaceborne thermal emission and reflection radiometer (ASTER) images. IEEE Trans. Geosci. Remote Sens. 36, 1113–1126.

Grace, J., Jose, J.S., Meir, P., Miranda, H.S., Montes, R.A., 2006. Productivity and carbon fluxes of tropical savannas. J. Biogeogr. 33, 387–400. https://doi.org/10.1111/j.1365-2699.2005.01448.x.

Grömping, U., 2006. Relative importance for linear regression in R: the package relaimpo. J. Stat. Softw. 17, 1–27.

Haario, H., Laine, M., Mira, A., Saksman, E., 2006. DRAM: efficient adaptive MCMC. Stat. Comput. 16, 339–354. https://doi.org/10.1007/s11222-006-9438-0.

Hollinger, D.Y., Richardson, A.D., 2005. Uncertainty in eddy covariance measurements and its application to physiological models. Tree Physiol. 25, 873–885.

Hollinger, D.Y., Aber, J., Dail, B., Davidson, E.A., Goltz, S.M., Hughes, H., Leclerc, M.Y., Lee, J.T., Richardson, A.D., Rodrigues, C., Scott, N.A., Achuatavarier, D., Walsh, J., 2004. Spatial and temporal variability in forest-atmosphere CO2 exchange. Glob. Change Biol. 10, 1689–1706. https://doi.org/10.1111/j.1365-2486.2004.00847.x.

Hsieh, C.I., Katul, G., Chi, T., 2000. An approximate analytical model for footprint estimation of scaler fluxes in thermally stratified atmospheric flows. Adv. Water Resour. 23, 765–772.

Huete, A., Didan, K., Miura, T., Rodriguez, E.P., Gao, X., Ferreira, L.G., 2002. Overview of the radiometric and biophysical performance of the MODIS vegetation indices. Remote Sens. Environ. 83, 195–213.

Kessomkiat, W., Franssen, H.J.H., Graf, A., Vereecken, H., 2013. Estimating random errors of eddy covariance data: an extended two-tower approach. Agric. For. Meteorol. 171, 203–219. https://doi.org/10.1016/j.agrformet.2012.11.019.

Kljun, N., Calanca, P., Rotach, M.W., Schmid, H.P., 2015. A simple two-dimensional parameterisation for flux footprint prediction (FFP). Geosci. Model Dev. 8, 3695–3713. https://doi.org/10.5194/gmd-8-3695-2015.

Kolle, O., Rebmann, C., 2009. EddySoft: Documentation of a Software Package to Acquire and Process Eddy Covariance Data. pp. 10.

Lasslop, G., Reichstein, M., Kattge, J., Papale, D., 2008. Influences of observation errors in eddy flux data on inverse model parameter estimation. Biogeosciences 5, 1311–1324.

Legendre, P., Legendre, L. (Eds.), 1998. Numerical Ecology, 2nd edition. Elsevier. https://doi.org/10.1016/S0167-8892(98)80066-3.

Ma, S., Baldocchi, D.D., Xu, L., Hehn, T., 2007. Inter-annual variability in carbon dioxide exchange of an oak/grass savanna and open grassland in California. Agric. For. Meteorol. 147, 157–171. https://doi.org/10.1016/j.agrformet.2007.07.008.

Mauder, M., Foken, T., 2011. Dokumentation and Instruction Manual of the Eddy-Covariance Software Package TK3. Universität Bayreuth, Abteilung Mikrometeorologie, Arbeitsergebnisse, pp. 46.

McDowell, N., Pockman, W.T., Allen, C.D., Breshears, D.D., Cobb, N., Kolb, T., Plaut, J., Sperry, J., West, A., Williams, D.G., Yepez, E.A., 2008. Mechanisms of plant survival and mortality during drought: why do some plants survive while others succumb to drought? New Phytol. 178, 719–739. https://doi.org/10.1111/j.1469-8137.2008.02436.x.

Migliavacca, M., Perez-Priego, O., Rossini, M., El-Madany, T.S., Moreno, G., van der Tol, C., Rascher, U., Berninger, A., Bessenbacher, V., Burkart, A., Carrara, A., Fava, F., Guan, J.-H., Hammer, T.W., Henkel, K., Juarez-Alcalde, E., Julitta, T., Kolle, O., Martín, M.P., Musavi, T., Pacheco-Labrador, J., Pérez-Burgueño, A., Wutzler, T., Zaehle, S., Reichstein, M., 2017. Plant functional traits and canopy structure control the relationship between photosynthetic CO2 uptake and far-red sun-induced fluorescence in a Mediterranean grassland under different nutrient availability. New Phytol. https://doi.org/10.1111/nph.14437.

Moncrieff, J.B., Massheder, J.M., deBruin, H., Elbers, J., Friborg, T., Heusinkveld, B., Kabat, P., Scott, S., Soegaard, H., Verhoef, A., 1997. A system to measure surface fluxes of momentum, sensible heat, water vapour and carbon dioxide. J. Hydrol. 189, 589–611.

Moncrieff, J., Clement, R., Finnigan, J., Meyers, T., 2004. Averaging, detrending, and filtering of eddy covariance time series. In: Lee, X., Massman, W.J., Law, B.E. (Eds.), Handbook of Micrometeorology: A Guide for Surface Flux Measurement and Analysis. Kluwer Academic Publishers, Dordrecht, pp. 7–31.

Moore, C.E., Beringer, J., Evans, B., Hutley, L.B., McHugh, I., Tapper, N.J., 2016. The contribution of trees and grasses to productivity of an Australian tropical savanna. Biogeosciences 13, 2387–2403. https://doi.org/10.5194/bg-13-2387-2016.

Nagler, P.L., Glenn, E.P., Kim, H., Emmerich, W., Scott, R.L., Huxman, T.E., Huete, A.R., 2007. Relationship between evapotranspiration and precipitation pulses in a semiarid rangeland estimated by moisture flux towers and MODIS vegetation indices. J. Arid. Environ. 70, 443–462. https://doi.org/10.1016/j.jaridenv.2006.12.026.

Otieno, D., Ondier, J., Arnhold, S., Okach, D., Ruidisch, M., Lee, B., Kolb, A., Onyango, J., Huwe, B., 2015. Patterns of CO2 exchange and productivity of the herbaceous vegetation and trees in a humid savanna in western Kenya. Plant Ecol. 216, 1441–1456. https://doi.org/10.1007/s11258-015-0523-3.

Paço, T.A., David, T.S., Henriques, M.O., Pereira, J.S., Valente, F., Banza, J., Pereira, F.L., Pinto, C., David, J.S., 2009. Evapotranspiration from a Mediterranean evergreen oak savannah: the role of trees and pasture. J. Hydrol. 369, 98–106. https://doi.org/10.1016/j.jhydrol.2009.02.011.

Papale, D., Reichstein, M., Aubinet, M., Canfora, E., Bernhofer, C., Kutsch, W., Longdoz, B., Rambal, S., Valentini, R., Vesala, T., Yakir, D., 2006. Towards a standardized processing of net ecosystem exchange measured with eddy covariance technique: algorithms and uncertainty estimation. Biogeosciences 3, 571–583.

Pereira, J.S., Mateus, J.A., Aires, L.M., Pita, G., Pio, C., David, J.S., Andrade, V., Banza, J., David, T.S., Paco, T.A., Rodrigues, A., 2007. Net ecosystem carbon exchange in three contrasting Mediterranean ecosystems – the effect of drought. Biogeosciences 4, 791–802.

Perez-Priego, O., Guan, J., Rossini, M., Fava, F., Wutzler, T., Moreno, G., Carvalhais, N., Carrara, A., Kolle, O., Julitta, T., Schrumpf, M., Reichstein, M., Migliavacca, M., 2015. Sun-induced chlorophyll fluorescence and photochemical reflectance index improve remote-sensing gross primary production estimates under varying nutrient availability in a typical Mediterranean savanna ecosystem. Biogeosciences 12, 6351–6367. https://doi.org/10.5194/bg-12-6351-2015.

Quero, J.L., Sterck, F.J., Martínez-Vilalta, J., Villar, R., 2011. Water-use strategies of six co-existing Mediterranean woody species during a summer drought. Oecologia 166, 45–57. https://doi.org/10.1007/s00442-011-1922-3.

R Development Core Team, 2015. R: A Language and Environment for Statistical Computing.

Rannik, U., Kolari, P., Vesala, T., Hari, P., 2006. Uncertainties in measurement and modelling of net ecosystem exchange of a forest. Agric. For. Meteorol. 138, 244–257. https://doi.org/10.1016/j.agrformet.2006.05.007.

Rannik, Ü., Peltola, O., Mammarella, I., 2016. Random uncertainties of flux measurements by the eddy covariance technique. Atmos. Meas. Tech. Discuss. 1–31. https://doi.org/10.5194/amt-2016-31.

Rebmann, C., Gockede, M., Foken, T., Aubinet, M., Aurela, M., Berbigier, P., Bernhofer, C., Buchmann, N., Carrara, A., Cescatti, A., Ceulemans, R., Clement, R., Elbers, J.A., Granier, A., Grunwald, T., Guyon, D., Havrankova, K., Heinesch, B., Knohl, A., Laurila, T., Longdoz, B., Marcolla, B., Markkanen, T., Miglietta, F., Moncrieff, J., Montagnani, L., Moors, E., Nardino, M., Ourcival, J.M., Rambal, S., Rannik, U., Rotenberg, E., Sedlak, P., Unterhuber, G., Vesala, T., Yakir, D., 2005. Quality analysis applied on eddy covariance measurements at complex forest sites using footprint modelling. Theor. Appl. Climatol. 80, 121–141. https://doi.org/10.1007/s00704-004-0095-y.

Reichstein, M., Falge, E., Baldocchi, D., Papale, D., Aubinet, M., Berbigier, P., Bernhofer, C., Buchmann, N., Gilmanov, T., Granier, A., Grunwald, T., Havrankova, K., Ilvesniemi, H., Janous, D., Knohl, A., Laurila, T., Lohila, A., Loustau, D., Matteucci, G., Meyers, T., Miglietta, F., Ourcival, J.-M., Pumpanen, J., Rambal, S., Rotenberg, E., Sanz, M., Tenhunen, J., Seufert, G., Vaccari, F., Vesala, T., Yakir, D., Valentini, R., 2005. On the separation of net ecosystem exchange into assimilation and ecosystem respiration: review and improved algorithm. Glob. Change Biol. 11, 1424–1439. https://doi.org/10.1111/j.1365-2486.2005.001002.x.

Richards, J.A., 2013. Remote Sensing Digital Image Analysis. Springer, Berlin Heidelberg, Berlin, Heidelberg.

Richardson, A.D., Aubinet, M., Barr, A.G., Hollinger, D.Y., Ibrom, A., Lasslop, G., Reichstein, M., 2012. Uncertainty quantification. Eddy Covariance: A Practical Guide to Measurement and Data Analysis. Springer, Dordrecht, pp. 173–210.

Rouse Jr, J., Haas, R.H., Schell, J.A., Deering, D.W., 1974. Monitoring Vegetation Systems in the Great Plains with ERTS.

Schmid, H.P., 2002. Footprint modeling for vegetation atmosphere exchange studies: a review and perspective. Agric. For. Meteorol. 113, 159–183.

Scholes, R.J., Archer, S.R., 1997. Tree-grass interactions in savannas 1. Annu. Rev. Ecol. Syst. 28, 517–544.

Sobrino, J.A., Jiménez-Muñoz, J.C., Zarco-Tejada, P.J., Sepulcre-Cantó, G., de Miguel, E., 2006. Land surface temperature derived from airborne hyperspectral scanner thermal infrared data. Remote Sens. Environ. 102, 99–115. https://doi.org/10.1016/j.rse.2006.02.001.

Tagesson, T., Fensholt, R., Cropley, F., Guiro, I., Horion, S., Ehammer, A., Ardö, J., 2015. Dynamics in carbon exchange fluxes for a grazed semi-arid savanna ecosystem in West Africa. Agric. Ecosyst. Environ. 205, 15–24. https://doi.org/10.1016/j.agee.2015.02.017.

Unger, S., Máguas, C., Pereira, J.S., David, T.S., Werner, C., 2012. Interpreting post-drought rewetting effects on soil and ecosystem carbon dynamics in a Mediterranean oak savannah. Agric. For. Meteorol. 154–155, 9–18. https://doi.org/10.1016/j.agrformet.2011.10.007.

Vickers, D., Mahrt, L., 1997. Quality control and flux sampling problems for tower and aircraft data. J. Atmos. Oceanic Technol. 14, 512–526.

Wang, Y.P., Kowalczyk, E., Leuning, R., Abramowitz, G., Raupach, M.R., Pak, B., van Gorsel, E., Luhar, A., 2011. Diagnosing errors in a land surface model (CABLE) in the time and frequency domains. J. Geophys. Res. 116, G01034. https://doi.org/10.1029/2010JG001385.

Wienhold, F.G., Welling, M., Harris, G.W., 1995. Micrometeorological measurement and source region analysis of nitrous-oxide fluxes from an agricultural soil. Atmos. Environ. 29, 2219–2227.

Wilczak, J.M., Oncley, S.P., Stage, S.A., 2001. Sonic anemometer tilt correction algorithms. Boundary Layer Meteorol. 99, 127–150.

Williams, M., Richardson, A.D., Reichstein, M., Stoy, P.C., Peylin, P., Verbeeck, H., Carvalhais, N., Jung, M., Hollinger, D.Y., Kattge, J., Leuning, R., Luo, Y., Tomelleri, E., Trudinger, C.M., Wang, Y.P., 2009. Improving land surface models with FLUXNET data. Biogeosciences 6, 1341–1359.

Wutzler, T., Moffat, A.M., Migliavacca, M., Knauer, J., Sickel, Kerstin, Šigut, Ladislav, Menzer, O., Reichstein, M., 2018. Basic and extensible post-processing of eddy covariance flux data with REddyProc. Biogeosci. Discuss n.d. Discuss 2018.